Analysis of Gaussian phase noise effects in DFT-s-OFDM systems for sub-THz transmissions

Yaya Bello[1*] , Jean-Baptiste Doré[1*] and David Demmer[1]

*Correspondence:
yaya.bello@cea.fr; jean-baptiste.
dore@cea.fr

[1] Univ. Grenoble Alpes, CEA-Leti,
38000, Grenoble, France

Abstract

The future generations of communication technologies envision the transmission of signals across the millimeter wave and sub-THz spectrums. However, the characteristics of the propagation channel at such high frequencies differ from what is observed in the conventional low-frequency spectrum with for instance, the apparition of stronger phase noise (PN) induced by the Radio Frequency (RF) transceivers and more especially by the oscillators. That is why there is growing interest in evaluating and adapting the 5G new radio (5G-NR) physical layer to the presence of PN. This article is dedicated to the study of discrete Fourier transform-spread-Orthogonal Frequency Division Multiplexing (DFT-s-OFDM) under uncorrelated Gaussian PN (GPN) impairments. We show that the presence of GPN induces two distortions: (i) a frequency-dependent random rotation of data, namely the subcarrier phase error (SPE) and (ii) a frequency-dependent intercarrier interference (ICI) that are analytically expressed. Then, we investigate the design of the adapted and optimal detection criterion according to the baseband model we derived in this paper. We demonstrate that (i) the proposed polar detector outperforms the conventional Euclidean detector and (ii) contrary to legacy OFDM, DFT-s-OFDM is a promising solution when strong GPN is involved.

Keywords: Beyond 5G, 6G, 3GPP, Uncorrelated phase noise, Optimal detector, Channel performance evaluation

1 Introduction

The deployment of cellular technologies in wider bandwidths at higher frequencies is an appealing solution to increase the capacity of wireless transmissions. The "sub-THz" spectrum ([100–300] GHz) is identified as a potential candidate for 6G [1]. Indeed, total but fragmented bandwidth of 58.6 GHz has been identified [2]. The 5G New Radio (5G-NR) standard today covers transmissions up to 71 GHz [3]. However, the 3rd generation partnership project (3GPP) is looking forward to the use of new spectrum for future releases. On the one hand, the IEEE 802.15.3d specification standardizes a Single-Carrier (SC) waveform with carrier aggregation [1]. On the other hand, research is being conducted to study how 5G-NR Multi-Carrier (MC) waveforms such as Orthogonal

Bello *et al. J Wireless Com Network*   (2024) 2024:60

Page 2 of 29

Frequency Division Multiplexing (OFDM) or discrete Fourier transform (DFT)-spread-OFDM (DFT-s-OFDM) can be adapted to the specificities of the sub-THz bands [4].

OFDM is a MC waveform standardized in 4G and 5G-NR for wireless transmissions. It consists in sending the signal simultaneously on many orthogonal subcarriers by using fast Fourier transform (FFT) [5]. OFDM reduces the design complexity of equalizers by allowing a "1-tap" channel equalization per subcarrier in the frequency-domain[1] [6]. However, the main drawback of OFDM is its high Peak-to-Average Power Ratio (PAPR) [7] which puts a lot of constraints on the Power Amplifier (PA). If the advantages of OFDM have to be maintained, the use of the DFT-s-OFDM seems to be a good compromise. The waveform is also standardized in 4G and 5G-NR but rather for uplink transmissions and also a candidate for sub-THz [8]. It can be seen as a DFT-precoded OFDM and emulates a SC system. It thus offers a lower PAPR compared to OFDM [9] and allows to operate PAs with reduced power back off, resulting in a higher energy efficiency [10].

Transmitting in the sub-THz bands presents some specific impairments such as the Phase Noise (PN) which is mainly generated by the high frequency oscillators suffering from random and short-term frequency instabilities. This phenomenon may lead to synchronization issues in clocked and sampled-data digital systems, as documented in [11]. The severity of PN amplifies as the carrier frequency increases, posing a significant threat to system performance transmitting in sub-THz bands. The induced effects of PN on OFDM transmission have been massively studied [12–15]. It has been proved that PN causes a common symbol rotation to all subcarriers, namely common phase error (CPE), and additive InterCarrier Interference (ICI). To correct the CPE, Phase Tracking Reference Signals (PT-RS) have been introduced in 5G-NR [15, 16]. However, dealing with the ICI remains tricky and requires sophisticated cancellation techniques [17]. That is the reason why ICI mitigation techniques have been proposed in recent literature [17–19]. However, those techniques cannot be directly extended to the DFT-s-OFDM systems because they rely on the presence of the CPE which is no longer the case with DFT-s-OFDM. In [8], the authors show that increasing the ICS up to 3840 kHz for DFT-s-OFDM systems, provides enhanced robustness against PN. However, increasing the InterCarrier Spacing (ICS) implies shortening the CP duration which results in lowered robustness against delay spread in the case of multi-path channel [20] or reduce the system's ability to handle time synchronization errors. It should also be mentioned that 5 G-NR standard imposes a minimum number of sub-carriers to be allocated. If this constraint is maintained, increasing the ICS necessarily implies increasing the bandwidth and the sampling frequency. PN mitigation in DFT-s-OFDM is discussed in [15, 21, 22]. Additionally, works were carried to enhance the channel estimation in the context of OFDM by proposing new PT-RS scheme [18].

1.1 Related state-of-the-art and motivations

PN can be modeled in various ways. Indeed, the PN can be defined as the sum of multiple noises [23]: some with a correlated nature, such as Wiener noise, and others

---

[1] By assuming the Cyclic Prefix (CP) size is higher than the channel delay spread and assuming a frequency-selective channel.

Table 1 Summary of the state-of-the-art phase noise mitigation techniques

	Correlated phase noise	Gaussian phase noise
Single Carrier	Modulation optim. (APSK based) e.g. [35] Interpolation [36, 37] DCT [38]	Modulation optim. [30, 39] Receiver optim. [29, 31]
OFDM	CPE [13] ICI cancellation [17] Time Domain [40]	Not addressed—part of this work
DFT-s-OFDM	Scheme inherited from SC Interpolation [41]	Not addressed—part of this work

The references cited here are not exhaustive, but provide an overview of recent works or important contributions on the subject related to the work presented in this communication

without, like the white Gaussian noise. Many studies consider models with correlated nature [4, 12, 14, 17, 18] such as the Wiener PN [22] and the 3GPP PN models [24]. The correlated nature of the PN allows to track and thus to compensate its correlated part to limit its impact on the radio link performance [25]. However, when the signal bandwidth is very large as planned for sub-THz and THz communications, the impact of the Gaussian nature of the PN becomes dominant [23]. It occurs: i) when the oscillator corner frequency remains small compared to the system bandwidth and ii) when the signal duration is short enough to fulfill the criterion presented in [23]. Those observations have been made at 200 GHz with a high-frequency oscillator presented in [26] and the simplified PN model detailed in [27].

As the system bandwidths are expected to grow for 6G transmissions in upper mmWave and sub-THz transmissions [28], the question of the design of physical layer robust to white Gaussian PN (GPN) rises. In this context, many studies focus on SC systems with constellation optimizations [29, 30], optimal detection criterion [31] and performance evaluation and comparison [32]. MC systems are also considered which is more in line with the 3GPP vision. Link and system performance of the OFDM and DFT-s-OFDM have been evaluated under GPN channels [33]. However, the GPN effects on MC systems are not yet comprehensively understood especially for DFT-s-OFDM systems. That is the reason why, we propose in this work to better study the effects of GPN on DFT-s-OFDM systems. The correlated nature of the PN will be thus considered fully and ideally compensated. Needless to mention that, in practice, perfect compensation is not feasible [34]. But in this work, it will be assumed that state-of-the-art algorithms are sufficiently efficient to make the correlated PN negligible compared to GPN. Table 1 provides a brief summary of PN compensation techniques presented in the literature for different waveforms, and highlights the interest of the work presented in this paper.

Overall, the main contributions of this paper can be described as follows:

1. We model the distortions induced by the GPN on the received DFT-s-OFDM baseband signal.
2. We develop a novel detection criterion adapted to DFT-s-OFDM systems in the presence of GPN by assuming the high Signal-to-Interference-plus-Noise Ratio (SINR) approximation.
3. We propose a sub-optimal implementation of the proposed detector more suitable for realistic systems [29].

4. We evaluate the link performance of a DFT-s-OFDM systems and compare them with legacy OFDM (in terms of packet error rates with 5G-NR channel coding techniques). To provide a fair comparison between the MC techniques, ICI mitigation techniques proposed for the OFDM [17] will be considered.

The remainder of the paper is as follows. In Sect. 2.1, we present the system model. Section 2.2 provides the analysis of the baseband received signal impaired by GPN. Detection criteria are derived in Sect. 3.1. Simulation results and comparison with state-of-the-art techniques are carried out in Sect. 3.2. A discussion is opened in Sect. 4 and finally, we end up with the conclusion in Sect. 5.

1.2 Notations

In what follows, underlined lower boldface letters, $\underline{\mathbf{a}}$, indicate column vectors, with a_k denoting the kth element of the column vector. The terms $\mathbf{diag}\{\mathbf{A}\}$ and $\mathbf{diag}_k\{\mathbf{A}\}$ respectively denote the diagonal and the kth element of the diagonal of the matrix $\mathbf{A}$. The term $\mathbb{E}[\cdot]$ denotes the expectation operator of the argument. The term $\mathbf{A}^{-1}$ represents the inverse of the matrix $\mathbf{A}$. The symbols $\mathfrak{Re}\{\cdot\}$, $\mathfrak{Im}\{\cdot\}$, $(\cdot)^*$ and $(\cdot)^H$ respectively denote the real part, the imaginary part, the conjugate and the transpose-conjugate of the argument. The operator $\odot$ and the symbol $\|\cdot\|$ respectively represent the Hadamard product and the norm operator. $\underline{\mathbf{a}}_\rho$ (resp. $\underline{\mathbf{a}}_\theta$) represents the column vector which contains all the magnitude values (resp. the phase values) of the vector $\underline{\mathbf{a}}$. The term a_{k_ρ} (resp. a_{k_θ}) denotes the magnitude value (resp. phase value) of the symbol a_k. The symbols $\det(\cdot)$ and $\cdot$ respectively denote the determinant value of the argument and the product operator. $\mathbf{N}_X$ indicates matrices of size $X \times X$ that fully contain the number $\mathbf{N}$. The term $\mathbf{F}_X$ is the DFT matrix of size X defined as:

$$\mathbf{F}_X^{(i,k)} = \frac{1}{\sqrt{X}} e^{-j2\pi \frac{(i-1)(k-1)}{X}}. \tag{1}$$

2 Methods

2.1 System model

2.1.1 Channel model

A coherent communication receiver with perfect time/frequency synchronization will be assumed in this work. The radio propagation channels in sub-THz frequencies are expected to be sparse [42]. It has been demonstrated that the Line-of-Sight (LoS) provides most of the energy contribution in sub-THz scenarios [42, 43]. It can be achieved by the use of high gain directional antennas which spatially filter the channel. Hence, we will assume a LoS-only propagation channel in this paper.

2.1.2 PN model

Regarding the PN model, we consider an uncorrelated GPN model. The phase error induced by the GPN can be modeled as follows

$$\phi[\tau] \backsim \mathcal{N}(0, \sigma_\phi^2), \tag{2}$$

where σ_ϕ^2 denotes the sum variance of the Tx and Rx GPNs, i.e.,

Table 2 Evaluation of K_0 depending on signal bandwidth and GPN regime

		System bandwidth B_W		
GPN regime	Power σ_ϕ^2	3.686 GHz	7.372 GHz	14.744 GHz
Strong GPN	10^{-1}	−108.67 dBc/Hz	−111.69 dBc/Hz	−114.70 dBc/Hz
Medium GPN	$5 \cdot 10^{-2}$	−111.67 dBc/Hz	−114.70 dBc/Hz	−117.71dBc/Hz
Low GPN	10^{-2}	−118.68 dBc/Hz	−121.69 dBc/Hz	−124.70 dBc/Hz

$$
\begin{aligned}
\sigma_\phi^2 &= \sigma_{\phi_{TX}}^2 + \sigma_{\phi_{RX}}^2 \\
&= 2K_0 B_W.
\end{aligned}
\tag{3}
$$

The term K_0 represents the power spectral density (PSD) of the generated GPN and B_W the bandwidth. For GPN, the phase error is white which means that its PSD is independent of the frequency. Regarding the bandwidth, it can be expressed as function of MC parameters $B_W = N_s \Delta_f$ where N_s denotes the DFT size block and Δ_f the ICS. The model (3) is based on the channel model considered in Sect. 2.1.1, i.e., absence of multipath components. Three levels of GPN regimes are considered in this work as detailed in Table 2.

### 2.1.3 DFT-s-OFDM waveform with the presence of PN

The expression of the baseband discrete-time received signal impaired by the GPN at the kth subcarrier is expressed as follows

$$
r_k = s_k \beta(k, N_s, N_f, \phi) \; + \; \gamma(k, N_s, N_f, \phi) + \; \eta(k, N_s, N_f),
\tag{4}
$$

where s_k is the transmitted signal at the kth subcarrier and N_f is the Fast Fourier Transform (FFT) block size. The terms $\beta(k, N_s, N_f, \phi)$, $\gamma(k, N_s, N_f, \phi)$ and $\eta(k, N_s, N_f)$ are, respectively, the channel coefficient, the additive ICI and the thermal noise after Fourier transformations at the receiver and are defined in (5) by

$$
\beta(k, N_s, N_f, \phi) = \frac{1}{N_s} \frac{1}{N_f} \sum_{f=0}^{N_s-1} \sum_{m=0}^{N_s-1} \sum_{p=0}^{N_f-1} e^{j2\pi \frac{(m-f)}{N_f}p} e^{-j2\pi \frac{(m-f)}{N_s}k} e^{j\phi_p}
$$

$$
\gamma(k, N_s, N_f, \phi) = \frac{1}{N_s} \frac{1}{N_f} \sum_{n=0, n \neq k}^{N_s-1} s_n \sum_{f=0}^{N_s-1} \sum_{m=0}^{N_s-1} \sum_{p=0}^{N_f-1} e^{j2\pi \frac{(m-f)}{N_f}p} e^{j2\pi \frac{kf-nm}{N_s}} e^{j\phi_p}
\tag{5}
$$

$$
\eta(k, N_s, N_f) = \frac{1}{\sqrt{N_s}} \frac{1}{\sqrt{N_f}} \sum_{f=0}^{N_s-1} \sum_{p=0}^{N_f-1} n_p e^{-j2\pi \frac{fp}{N_f}} e^{j2\pi \frac{kf}{N_s}}.
$$

The term $n_p \backsim \mathbb{CN}\left(0, \sigma_n^2\right)$ represents the discrete-time thermal noise in time-domain which follows an independent and identically distributed complex Gaussian random process of zero-mean and variance σ_n^2. The term $\eta(k, N_s, N_f)$ is the thermal noise after Fourier transformations at the receiver. To illustrate the baseband model (4) and to compare it with the equivalent SC and OFDM models, we represent in Fig. 1 the probability of the Error Vector Magnitude obtained for the different waveforms under strong GPN regime and without thermal noise. Yellow areas denote the region of highly

(a) SC   (b) OFDM
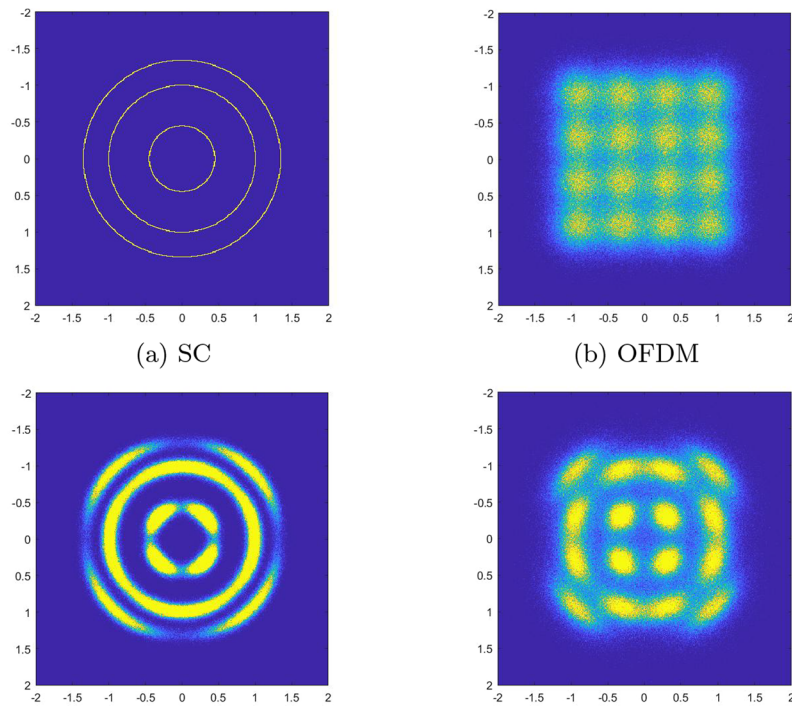
(c) DFT-s-OFDM at subcarrier $k = 1$ (d) DFT-s-OFDM at subcarrier $k = 10$

Fig. 1 GPN distortion on 16-QAM modulated signal with SNR = 50 dB

probable occurrences and blue zones represent the regions of almost null probability of appearance.

One can observe that, with Fig. 1a, GPN only causes the rotation of the transmitted symbols for SC systems (without pulse shaping filter). Regarding OFDM systems, in Fig. 1b, the received constellation looks really noisy. The distortion is isotropic and results from the presence of ICI. Concerning the DFT-s-OFDM systems, the behavior is frequency-dependent (or subcarrier-dependent) and that is why we decided to illustrate with two distinct subcarriers $k = 1$ and $k = 10$. For the subcarrier $k = 1$, depicted in Fig. 1c, one can observe that the symbol rotation effect dominates the ICI effect. Whereas for the subcarrier $k = 10$, depicted in Fig. 1d, the ICI is stronger.

The OFDM model can thus not be directly extended to DFT-s-OFDM. That is the reason why we believe that studying the particularities of the DFT-s-OFDM model is worthy. We propose in the next section a probabilistic study of the distortion terms $\beta(k, N_s, N_f, \phi)$ and $\gamma(k, N_s, N_f, \phi)$.

2.2 Model analysis

In this section, we study the stochastic properties of distortion terms $\beta(k, N_s, N_f, \phi)$ and $\gamma(k, N_s, N_f, \phi)$. Thereafter, for sake of clarity, we denote $\beta_k = \beta(k, N_s, N_f, \phi)$, $\gamma_k = \gamma(k, N_s, N_f, \phi)$ and $\eta_k = \eta(k, N_s, N_f)$. The terms β_k and γ_k can be expressed as function of the one order Dirichlet kernel K and G as follows

Bello *et al. J Wireless Com Network*   (2024) 2024:60

Page 7 of 29

Table 3 Size of FFT and DFT blocks

	First configuration			
N_s	120	240	360	480
N_f	512			
$\zeta = N_s/N_f$	0.2344	0.4688	0.7031	0.9375
μ	9			
Δ_f [kHz]	7680			
B_W [GHz]	0.922	1.843	2.765	3.686

$$\beta(k, N_s, N_f, \phi) = \sum_{p=0}^{N_f-1} e^{j\phi_p} K_{N_s}^{N_s}\left(\frac{p}{N_f} - \frac{k}{N_s}\right) G_{N_f}^{N_s}\left(\frac{k}{N_s} - \frac{p}{N_f}\right)$$

$$\gamma(k, N_s, N_f, \phi) = \sum_{n=0, n\neq k}^{N_s-1} s_n \sum_{p=0}^{N_f-1} e^{j\phi_p} K_{N_s}^{N_s}\left(\frac{p}{N_f} - \frac{n}{N_s}\right) G_{N_f}^{N_s}\left(\frac{k}{N_s} - \frac{p}{N_f}\right),$$

(6)

where

$$K_X^P(y) = \frac{1}{X}\sum_{m=0}^{P-1} e^{j2\pi my} \quad \text{and} \quad G_X^P(z) = \frac{1}{X}\sum_{f=0}^{P-1} e^{j2\pi fz}.$$

(7)

According to these expressions, one can notice the dependence on the subcarrier index k, DFT spreading size N_s and FFT size N_f. One should not forget that the variables β_k and γ_k are functions of time as well (the time index is omitted in (6) for the sake of conciseness). The objective of the section is twofold: (i) determining their probability density functions and (ii) studying their dependence on the frequency (the subcarrier). For OFDM-like systems, the central limit theorem states that the random noises converge to the standard normal distribution when observed in the frequency domain (post-FFT at the receiver side). To verify this assumption, we estimate the mean value $m_X = \mathbb{E}[X[n]]$ and the variance $\sigma_X^2 = \mathbb{E}[|X[n] - m_X|^2]$ of the random complex sequences $X[n]$ (where n is the time index) and we apply a normality test. When it comes to the frequency dependence, the variations of the means and variances obtained for each subcarrier are analyzed. We propose to compare the maximum, minimum and arithmetic mean values. As long as those three values are almost equal, there is no dependence on frequency. On the contrary, if those values differ, it implies that the subcarriers do not experiences the same stochastic distortion i.e., a subcarrier-dependent behavior. Because the variables β_k and γ_k are complex, we propose to simplify the problem by analyzing their real coordinates. The polar representation has been preferred for β_k and the Cartesian[2] for γ_k. Two scenarios, namely first and second configurations, are defined in Tables 3 and 4.

---

[2] The choice of the system coordinate is quite clear from the study and for sake of simplicity we do not provide all the results but to give a hint as β_k represents a rotation and γ_k is an additive noise the respective choice for polar and Cartesian systems makes sense.

Bello *et al. J Wireless Com Network*   (2024) 2024:60

Page 8 of 29

Table 4 Size of FFT and DFT blocks

	Second configuration			
N_s	480	960	1920	3840
N_f	512	1024	2048	4096
$\zeta = N_s/N_f$	0.9375			
μ	9	8	7	6
Δ_f [kHz]	7680	3840	1920	960
B_W [GHz]	3.686			

2.2.1 Two evaluation scenarios

This first scenario aims at evaluating the impact of the system bandwidth B_W. To do so, we consider different DFT precoding sizes N_s for the DFT-s-OFDM with a constant ICS (i.e., a constant numerology[3]. index $\mu = 9$). The parameter list is given in Table 3.

The second configuration, detailed in Table 4, focuses on the impact of the ICS and on the ratio between the DFT size and the FFT size[4] denoted by $\zeta = \frac{N_s}{N_f}$. All configurations share the same GPN PSD level with $K_0 = -108.67$ dBc/Hz.

2.2.2 Stochastic properties of the subcarrier phase error

Let us express the term β_k in the following form

$$\beta_k = \rho_k e^{j\Phi_k}, \tag{8}$$

where ρ_k and Φ_k are, respectively, the magnitude and the phase of β_k. Therefore, one obtains the following mean and variance vectors

$$\underline{\boldsymbol{m}}_\rho = \left[m_{\rho_0}, \cdots, m_{\rho_{N_s-1}} \right]^T, \quad \underline{\boldsymbol{\sigma}}_\rho^2 = \left[\sigma_{\rho_0}^2, \cdots, \sigma_{\rho_{N_s-1}}^2 \right]^T$$
$$\underline{\boldsymbol{m}}_\Phi = \left[m_{\Phi_0}, \cdots, m_{\Phi_{N_s-1}} \right]^T, \quad \underline{\boldsymbol{\sigma}}_\Phi^2 = \left[\sigma_{\Phi_0}^2, \cdots, \sigma_{\Phi_{N_s-1}}^2 \right]^T. \tag{9}$$

First configuration: Fig. 2a, b presents the dependence of stochastic properties of ρ_k on the DFT spreading value N_s by depicting the variations of the maximum, the minimum and the arithmetic mean of $\underline{\boldsymbol{m}}_\rho$ and $\underline{\boldsymbol{\sigma}}_\rho^2$ as function of N_s. One can observe that the three curves are superimposed around 1 for the mean and around 0 (or rather a negligible value) for the variance. We can therefore conclude that ρ_k is a deterministic value equal to 1 for each subcarrier and whatever the DFT spreading value N_s is.

Figure 2c, d shows the similar study for $\underline{\boldsymbol{m}}_\Phi$ and $\underline{\boldsymbol{\sigma}}_\Phi^2$. In Fig. 2c, the three curves are also superimposed around 0. It implies that the rotation angle Φ_k is zero-mean for all subcarriers k and whatever the DFT spreading length N_s is. However, when one looks at the curves for the variances depicted on Fig. 2d, they can observe that the curves start standing out from $N_s = 240$ and the difference between the maximum and minimum values increases with N_s. It means that:

---

[3] Numerology is a feature introduced in 5G-NR and corresponds to the ICS Δ_f is the following $\Delta_f = 15 \times 2^\mu$ kHz [44]

[4] N_s also denotes the size of the inverse DFT (IDFT) despreading block size and N_f the inverse FFT (IFFT) block size.
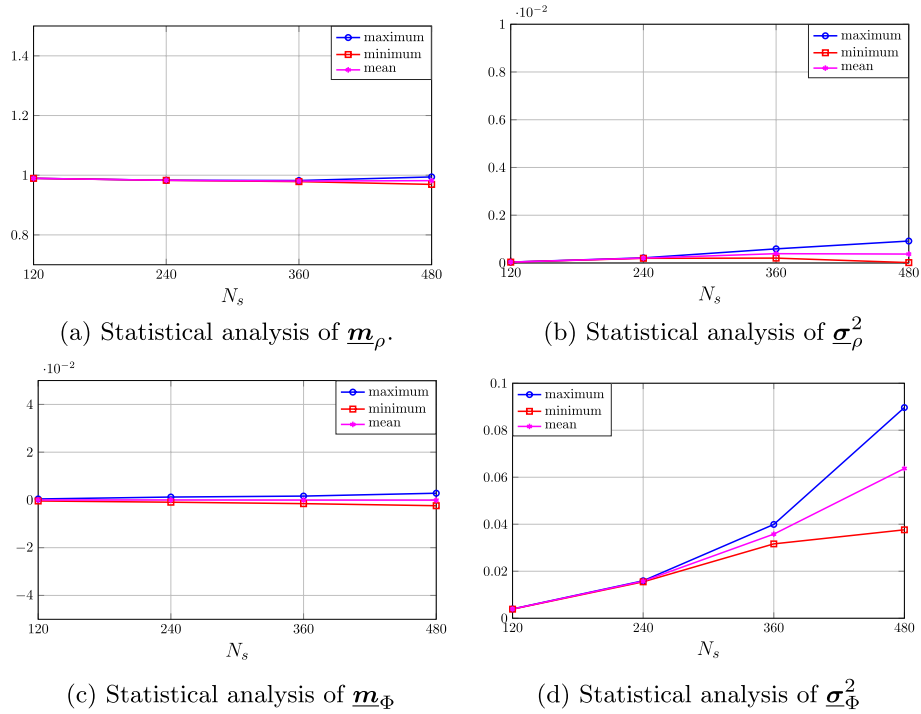
(a) Statistical analysis of $\underline{\boldsymbol{m}}_{\rho}$.

(b) Statistical analysis of $\underline{\boldsymbol{\sigma}}^2_{\rho}$

(c) Statistical analysis of $\underline{\boldsymbol{m}}_{\Phi}$

(d) Statistical analysis of $\underline{\boldsymbol{\sigma}}^2_{\Phi}$

Fig. 2 Statistical analysis of ρ_k and Φ_k using the First configuration

- for $\zeta = \frac{N_s}{N_f} \le \frac{240}{512}$, the variances $\underline{\boldsymbol{\sigma}}^2_{\Phi}$ are frequency-independent and all the subcarriers experience the same random rotation. The behavior tends to what is observed for a classic OFDM system.

- otherwise, the variances $\underline{\boldsymbol{\sigma}}^2_{\Phi}$ are frequency-dependent, i.e., appearance of a subcarrier-dependent behavior. The subcarriers experience different random rotations, hence the name "subcarrier phase error" (SPE). This behavior is characteristic of DFT-s-OFDM and is not observed in classic OFDM systems.

Second configuration: Fig. 3 presents the stochastic analysis of ρ_k and Φ_k by considering the second configuration. By paying attention to the scales, one can notice that the stochastic parameters of $\underline{\boldsymbol{m}}_{\rho}$ remain frequency-independent and, thus ρ_k is a deterministic value equal to 1. Regarding $\underline{\boldsymbol{\sigma}}^2_{\Phi}$, the subcarrier-dependent behavior is this time observed for all the values of ζ. It means that Φ_k are zero-mean random rotations with a frequency-dependent variance. In addition to that, if one assesses the dependence on frequency by evaluating the difference between the maximum and minimum values, they can observe that it remains constant for all values of the ratio ζ. It implies that the variances of the rotation $\underline{\boldsymbol{\sigma}}^2_{\Phi}$ are actually functions of ζ. This observation was not expected from the analysis of the analytical expressions (6).

Gaussianity test: β_k is therefore reduced to a random rotation of angle Φ_k. In the previous paragraphs, we numerically estimated the mean and variance of the angles Φ_k as function of the ratio ζ. The aim of this paragraph is to validate the Gaussian distribution hypothesis. To do so, we consider a specific ratio $\zeta = 0.9375$ (with (N_s, N_f)
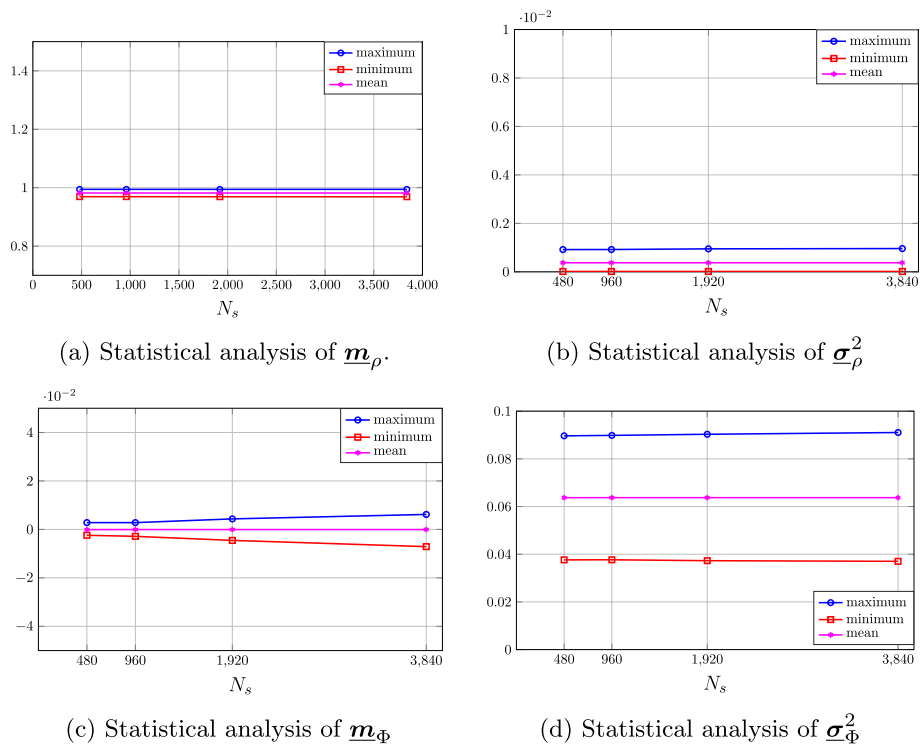
(a) Statistical analysis of $\underline{m}_\rho$.

(b) Statistical analysis of $\underline{\sigma}_\rho^2$

(c) Statistical analysis of $\underline{m}_\Phi$

(d) Statistical analysis of $\underline{\sigma}_\Phi^2$

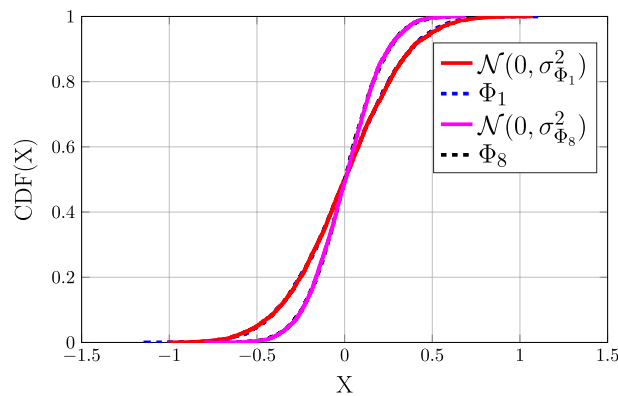**Fig. 3** Statistical analysis of ρ_k and Φ_k using the Second configuration
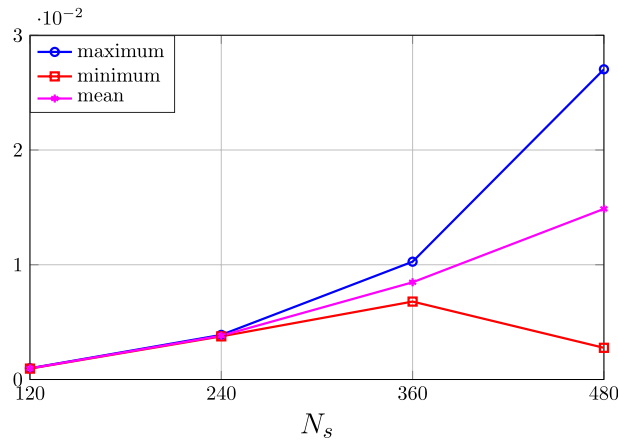

Fig. 4 CDF of Φ_k

$= (480, 512))$ and we compare the cumulative distribution function (CDF) of Φ_k with the CDF of a Gaussian random process (zero-mean and variance $\sigma_{\Phi_k}^2$).

The results are illustrated in Fig. 4 for two distinct subcarriers $k = \{1, 8\}$, chosen arbitrarily. One can notice the good matching between the CDFs of Φ_k and the equivalent Gaussian random distribution. To further validate the hypothesis, we perform a Kolmogorov–Smirnov test [45], with significance factor[5] $\alpha = 0.1$, to evaluate the Gaussianity property of simulated Φ_k. As expected, the test is validated and therefore we can

---

[5] It represents the validity factor of the Gaussianity test.

Bello *et al. J Wireless Com Network*   (2024) 2024:60

Page 11 of 29
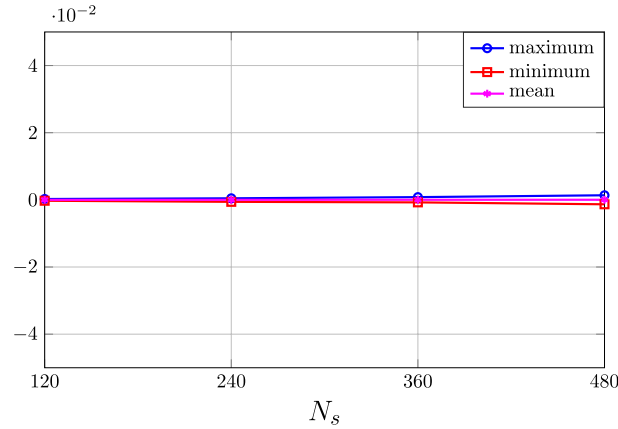
(a) Statistical analysis of $\underline{\boldsymbol{m}}_{\mathfrak{Re}\{\gamma\}}$.

(b) Statistical analysis of $\underline{\boldsymbol{\sigma}}^2_{\mathfrak{Re}\{\gamma\}}$

Fig. 5 Statistical analysis of $\mathfrak{Re}\{\gamma_k\}$ using the First configuration

assume that the SPE Φ_k follows an uncorrelated zero-mean Gaussian random process with a variance $\sigma^2_{\Phi_k}$

$$\Phi_k \frown \mathcal{N}(0, \sigma^2_{\Phi_k}), \forall k, \forall (N_s, N_f). \tag{10}$$

### 2.2.3 Stochastic properties of the intercarrier interference

In this paragraph, we study the stochastic properties and the distribution of the ICI term γ_k. To do so, we define the mean and variance of the real and imaginary parts

$$\underline{\boldsymbol{m}}_{\mathfrak{Re}\{\gamma\}} = \left[m_{\mathfrak{Re}\{\gamma_0\}}, \cdots, m_{\mathfrak{Re}\{\gamma_{N_s-1}\}} \right]^T, \quad \underline{\boldsymbol{\sigma}}^2_{\mathfrak{Re}\{\gamma\}} = \left[\sigma^2_{\mathfrak{Re}\{\gamma_0\}}, \cdots, \sigma^2_{\mathfrak{Re}\{\gamma_{N_s-1}\}} \right]^T$$

$$\underline{\boldsymbol{m}}_{\mathfrak{Im}\{\gamma\}} = \left[m_{\mathfrak{Im}\{\gamma_0\}}, \cdots, m_{\mathfrak{Im}\{\gamma_{N_s-1}\}} \right]^T, \quad \underline{\boldsymbol{\sigma}}^2_{\mathfrak{Im}\{\gamma\}} = \left[\sigma^2_{\mathfrak{Im}\{\gamma_0\}}, \cdots, \sigma^2_{\mathfrak{Im}\{\gamma_{N_s-1}\}} \right]^T. \tag{11}$$

Because the results for the real and imaginary parts are the same, only the analysis for the real part is presented hereafter.
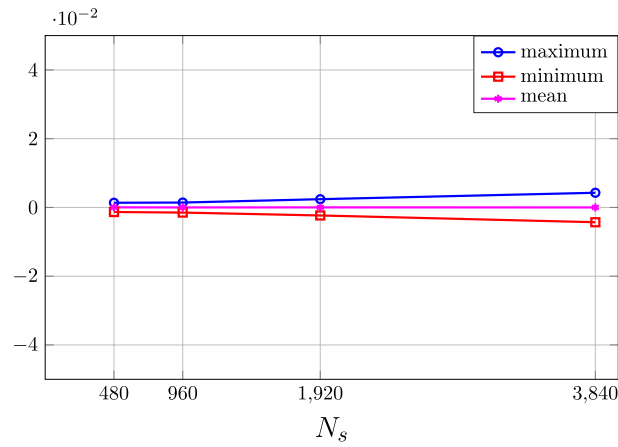
(a) Statistical analysis of $\underline{\boldsymbol{m}}_{\mathfrak{Re}\{\gamma\}}$.
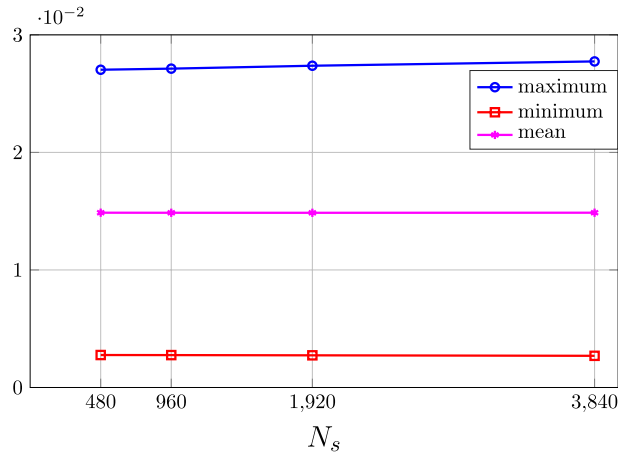
(b) Statistical analysis of $\underline{\boldsymbol{\sigma}}^2_{\mathfrak{Re}\{\gamma\}}$

Fig. 6 Statistical analysis of $\mathfrak{Re}\{\gamma_k\}$ using the Second configuration

First configuration: Fig. 5a, b presents the dependence of stochastic properties of $\mathfrak{Re}\{\gamma_k\}$ on the DFT spreading value N_s assuming the first configuration. One can observe that the real part of the ICI is a zero-mean random variable. Additionally:

- for $\zeta = \frac{N_s}{N_f} \leq \frac{240}{512}$, one can notice a frequency-independent variance, meaning that all the subcarriers experience the same random noise. The behavior tends to what is observed for a classic OFDM system.
- otherwise, the variances $\underline{\boldsymbol{\sigma}}^2_{\mathfrak{Re}\{\gamma\}}$ are frequency-dependent. The subcarriers experience a different random additive noise. This behavior is characteristic of DFT-s-OFDM and was not observed in classic OFDM systems.

As for the SPE (configuration 1), one can observe the subcarrier-dependent behavior of ICI increases with ζ.

Second configuration: With Fig. 6a, b, we analyze the stochastic property of the real part of the ICI for a constant ratio ζ. One can observe that the real part of the ICI is a zero-mean random variable with frequency-dependent variance. The difference between
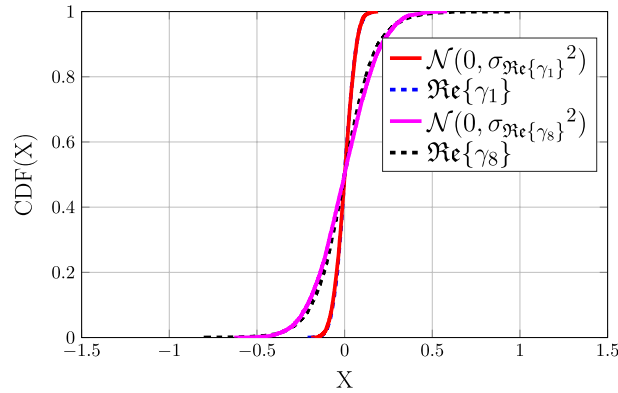
Bello *et al. J Wireless Com Network*   (2024) 2024:60

Page 13 of 29

Fig. 7 CDF of $\mathfrak{Re}\{\gamma_k\}$

the maximum and the minimum values is independent of the ratio ζ. It thus means that the variances of the real part of the ICI is function of the subcarrier index and the ratio ζ. This observation was not expected and is not trivial from the analytical expression (6).

Gaussianity test: γ_k is therefore a complex zero-mean random noise. In the previous paragraphs, we numerically estimated the mean and variance of its real part $\mathfrak{Re}\{\gamma_k\}$ as function of the ratio ζ. The objective of this paragraph is to validate the hypothesis of a Gaussian distribution. To do so, we consider a specific ratio $\zeta = 0.9375$ (with $(N_s, N_f) = (480, 512)$) and we compare the cumulative distribution function (CDF) of $\mathfrak{Re}\{\gamma_k\}$ with the CDF of a Gaussian random process (zero-mean and variance $\sigma^2_{\mathfrak{Re}\{\gamma_k\}}$). The results are illustrated in Fig. 7 for two distinct subcarriers $k = \{1, 8\}$, chosen arbitrarily. One can notice the curves do not perfectly match. Indeed, applying the Kolmogorov-Smirnov test (with the significance factor $\alpha = 0.1$) to determine if the variable γ_k follows an uncorrelated Gaussian distribution would result in the hypothesis being rejected. Thereby, the variable γ_k is correlated which is different compared to the previously studied SPE term Φ_k. The ICI correlated nature is expected and corresponds to the first sum of (6).

2.2.4 Lessons learnt

In this section, we characterized the term β_k and the ICI term γ_k. We showed that the term β_k corresponds to a random phase shift where the SPE (i.e., the phase of β_k) follows a zero-mean Gaussian random process. The variance of the SPE distribution depends on the ratio $\zeta = \frac{N_s}{N_f}$, the power of the PN σ^2_ϕ, and on the subcarrier index k (from a given ratio ζ). Moreover, the ICI is a zero-mean random variable with a correlated distribution. All these observations cannot be easily analytically studied. The expression (4) can be simplified as follows

$$r_k \simeq s_k e^{j\Phi_k} + \gamma_k + \eta_k. \tag{12}$$

The baseband model (12) is interesting because it reflects the compromise DFT-s-OFDM operates between SC and CP-OFDM. Indeed, one can observe i) the random rotation of the data, $e^{j\Phi_k}$, specific of SC systems [29, 30] and ii) the additive ICI, γ_k, characteristic of MC systems, such as OFDM systems [13]. For the CP-OFDM, a detector based on Euclidean distances is most suited because of the isotropic distribution of the

additive ICI and thermal noise [14]. When it comes to the SC case, specific detection criteria have been proposed, such as a detection in the polar domain [29, 30]. The question of the optimal detection criterion for DFT-s-OFDM systems with GPN impairments is therefore still open.

3 Results

3.1 Optimum demodulation in the presence of GPN

In this section, we derive an accurate detection criterion adapted to DFT-s-OFDM baseband model (12). For that, we can rewrite the expression (12) in a vector form as follows

$$\underline{\mathbf{r}} \simeq \underline{\mathbf{s}} \odot e^{j\underline{\boldsymbol{\Phi}}} + \underline{\mathbf{w}}, \tag{13}$$

with $\underline{\mathbf{r}} = [r_0, \cdots, r_{N_s-1}]^T$, $\underline{\mathbf{s}} = [s_0, \cdots, s_{N_s-1}]^T$ and $\underline{\boldsymbol{\Phi}} = [\Phi_0, \cdots, \Phi_{N_s-1}]^T$. The term $\underline{\mathbf{w}} = \underline{\boldsymbol{\eta}} + \underline{\boldsymbol{\gamma}}$ such that $\underline{\boldsymbol{\eta}} = [\eta_0, \cdots, \eta_{N_s-1}]^T$ and $\underline{\boldsymbol{\gamma}} = [\gamma_0, \cdots, \gamma_{N_s-1}]^T$, denotes the additive interference-plus-noise after DFT-s-OFDM demodulator including the thermal noise and the ICI term. The model of the baseband received signal (13) is similar to the model of a SC system in the presence of the PN $\underline{\boldsymbol{\Phi}}$ and an additive noise $\underline{\mathbf{w}}$. However, it seems important to remind that in the case of SC, the noise follows an independent complex Gaussian distribution while for the DFT-s-OFDM the ICI, and by extension the term $\underline{\mathbf{w}}$, exhibits a correlated nature. The authors in [29, 30] propose an optimal detector for a SC system impaired by GPN. We therefore propose to extend their results to DFT-s-OFDM systems. To do so, we need to explicit the probability distribution of the random rotation $\underline{\boldsymbol{\Phi}}$ and the additive interference-plus-noise term $\underline{\mathbf{w}}$.

3.1.1 Probability distribution

According to the results presented in Sect. 2.2, we define the SPE vector $\underline{\boldsymbol{\Phi}}$ as a real Gaussian vector with a mean $\underline{\mathbf{m}}_\Phi$ and a correlation matrix $\boldsymbol{\Gamma}_\Phi$ as follows

$$\underline{\boldsymbol{\Phi}} \backsim \mathcal{N}(\underline{\mathbf{m}}_\Phi, \boldsymbol{\Gamma}_\Phi) = \begin{cases} \underline{\mathbf{m}}_\Phi = \underline{\mathbf{0}}_{N_s} \\[1.5ex] \boldsymbol{\Gamma}_\Phi = \sigma_{\Phi_k}^2 \mathbf{I}_{N_s}, \end{cases} \tag{14}$$

where $\sigma_{\Phi_k}^2$,[6] is defined in (10) and $\mathbf{I}_{N_s}$ is the identity matrix with size $N_s \times N_s$. The noise vector $\underline{\mathbf{w}}$ is the sum of the thermal noise vector $\underline{\boldsymbol{\eta}}$ and the ICI vector $\underline{\boldsymbol{\gamma}}$. According to the linear property and power conservation of the Fourier transform, the thermal noise vector $\underline{\boldsymbol{\eta}}$ is defined as a complex Gaussian vector (independent and identically distributed) given by

$$\underline{\boldsymbol{\eta}} \backsim \mathbb{CN}(\underline{\mathbf{m}}_\eta, \boldsymbol{\Gamma}_\eta) = \begin{cases} \underline{\mathbf{m}}_\eta = \underline{\mathbf{0}}_{N_s} \\[1.5ex] \boldsymbol{\Gamma}_\eta = \sigma_n^2 \mathbf{I}_{N_s}, \end{cases} \tag{15}$$

where $\underline{\mathbf{m}}_\eta$ denotes the mean vector, $\boldsymbol{\Gamma}_\eta$ the correlation matrix and σ_n^2 the variance of the thermal noise. If one considers that the ICI follows a correlated complex Gaussian distribution, it leads to

---

[6] The SPE power $\sigma_{\Phi_k}^2$ can be obtained by taking the diagonal of the correlation matrix $\boldsymbol{\Gamma}_\Phi$, i.e. $\sigma_{\Phi_k}^2 = \mathbf{diag}_k\{\boldsymbol{\Gamma}_\Phi\}$.

$$\underline{\boldsymbol{\gamma}} \backsim \mathbb{CN}(\underline{\mathbf{m}}_\gamma, \boldsymbol{\Gamma}_\gamma) = \begin{cases} \underline{\mathbf{m}}_\gamma = \underline{\mathbf{0}}_{N_s} \\ \\ \boldsymbol{\Gamma}_\gamma = \boldsymbol{\Gamma}_\gamma, \end{cases} \tag{16}$$

where $\underline{\mathbf{m}}_\gamma$ is the mean vector and $\boldsymbol{\Gamma}_\gamma$ the correlation matrix of the ICI vector $\underline{\boldsymbol{\gamma}}$. Considering (15) and (16), the noise vector $\underline{\mathbf{w}}$ can be defined as a Gaussian vector with a mean vector $\underline{\mathbf{m}}_w$ and a correlation matrix $\boldsymbol{\Gamma}_w$ given by

$$\underline{\mathbf{w}} \backsim \mathbb{CN}(\underline{\mathbf{m}}_w, \boldsymbol{\Gamma}_w) = \begin{cases} \underline{\mathbf{m}}_w = \underline{\mathbf{0}}_{N_s} \\ \\ \boldsymbol{\Gamma}_w = \sigma_n^2 \mathbf{I}_{N_s} + \boldsymbol{\Gamma}_\gamma. \end{cases} \tag{17}$$

3.1.2 Optimal detection criterion

The Symbol Error Probability is minimized by the Maximum Likelihood (ML) decision criterion for equi-probable and independent symbols. The channel likelihood function can be written as follows [29, 30]

$$p(\underline{\mathbf{r}}|\underline{\mathbf{s}}) = p(\underline{\mathbf{r}}_\rho, \underline{\mathbf{r}}_\theta \mid \underline{\mathbf{s}}_\rho, \underline{\mathbf{s}}_\theta). \tag{18}$$

Thus, we have to express more clearly the ML decision criterion. Before studying the amplitude and phase of the received signal vector $\underline{\mathbf{r}}$, we denote $\underline{\mathbf{w}} \odot e^{-j(\underline{\boldsymbol{\Phi}}+\underline{\mathbf{s}}_\theta)}$ by $\underline{\mathbf{w}}'$. The term $\underline{\mathbf{w}}'$ has the same stochastic properties as $\underline{\mathbf{w}}$.[7] The amplitude of the received DFT-s-OFDM symbol is given by

$$\begin{aligned} \underline{\mathbf{r}}_\rho &= \left| (\underline{\mathbf{s}}_\rho + \underline{\mathbf{w}}') \odot e^{j(\underline{\boldsymbol{\Phi}}+\underline{\mathbf{s}}_\theta)} \right| \\ &= \sqrt{(\underline{\mathbf{s}}_\rho + \mathfrak{Re}\{\underline{\mathbf{w}}'\})^2 + \mathfrak{Im}\{\underline{\mathbf{w}}'\}^2}, \end{aligned} \tag{19}$$

and the phase by

$$\begin{aligned} \underline{\mathbf{r}}_\theta &= \arg\left((\underline{\mathbf{s}}_\rho + \underline{\mathbf{w}}') \odot e^{j(\underline{\boldsymbol{\Phi}}+\underline{\mathbf{s}}_\theta)} \right) \\ &= \underline{\mathbf{s}}_\theta + \underline{\boldsymbol{\Phi}} + \arctan\left(\mathfrak{Im}\{\underline{\mathbf{w}}'\} \odot (\underline{\mathbf{s}}_\rho + \mathfrak{Re}\{\underline{\mathbf{w}}'\})^{-1} \right). \end{aligned} \tag{20}$$

According to the demonstration of the high SINR approximation given in "Appendix 1", the expressions (19) and (20) become

$$\begin{cases} \underline{\mathbf{r}}_\rho - \underline{\mathbf{s}}_\rho \simeq \mathfrak{Re}\{\underline{\mathbf{w}}'\} \\ \\ \underline{\mathbf{r}}_\theta - \underline{\mathbf{s}}_\theta \simeq \underline{\boldsymbol{\Phi}} + \mathfrak{Im}\{\underline{\mathbf{w}}'\} \odot \underline{\mathbf{s}}_\rho^{-1}. \end{cases} \tag{21}$$

The symbol $\underline{\mathbf{s}}_\rho^{-1}$ is the vector containing the inverse of elements of $\underline{\mathbf{s}}_\rho$. The following terms $\mathfrak{Re}\{\underline{\mathbf{w}}'\}$ and $\underline{\boldsymbol{\Phi}} + \mathfrak{Im}\{\underline{\mathbf{w}}'\} \odot \underline{\mathbf{s}}_\rho^{-1}$ are, respectively, the additive noise in the amplitude channel and the additive Gaussian noise in the phase channel. In order to express the ML decision criterion in (18), we have to derive the Probability Density Function

---

[7] by assuming the complex Gaussian noise vector is circularly symmetric.

(PDF) of the expressions in (21). The PDF of the first expression can be expressed as follows

$$p(\underline{\mathbf{r}}_\rho \mid \underline{\mathbf{s}}_\rho) = \frac{1}{\sqrt{(2\pi)^{N_s} |\det(\mathfrak{Re}\{\mathbf{\Gamma}_w\})|}} \cdot e^{-\frac{1}{2}z}, \tag{22}$$

where $z = (\underline{\mathbf{r}}_\rho - \underline{\mathbf{s}}_\rho)^T \mathfrak{Re}\{\mathbf{\Gamma}_w\}^{-1}(\underline{\mathbf{r}}_\rho - \underline{\mathbf{s}}_\rho)$. When it comes to the phase domain, the term $\underline{\mathbf{\Phi}} + \mathfrak{Im}\{\underline{\mathbf{w}}'\} \odot \underline{\mathbf{s}}_\rho^{-1}$ is expressed as follows

$$\underline{\mathbf{\Phi}} + \mathfrak{Im}\{\underline{\mathbf{w}}'\} \odot \underline{\mathbf{s}}_\rho^{-1} \backsim \mathcal{N}(\underline{\mathbf{m}}, \mathbf{\Gamma}) = \begin{cases} \underline{\mathbf{m}} = \underline{\mathbf{0}}_{N_s} \\[2mm] \mathbf{\Gamma} = \mathbf{\Gamma}_\Phi + \mathfrak{Im}\{\mathbf{\Gamma}_w\} \odot \underline{\mathbf{s}}_\rho^{-2}. \end{cases} \tag{23}$$

Therefore, we can express the PDF of the second expression in (21) by

$$p(\underline{\mathbf{r}}_\theta \mid \underline{\mathbf{s}}_\theta) = \frac{1}{\sqrt{(2\pi)^{N_s} |\det(\mathbf{\Gamma})|}} \cdot e^{-\frac{1}{2}l}, \tag{24}$$

where $l = (\underline{\mathbf{r}}_\theta - \underline{\mathbf{s}}_\theta)^T \mathbf{\Gamma}^{-1}(\underline{\mathbf{r}}_\theta - \underline{\mathbf{s}}_\theta)$. From (22) and (24), the conditional PDF is written as

$$p(\underline{\mathbf{r}} \mid \underline{\mathbf{s}}) = \frac{e^{\left(-\frac{1}{2}(z+l)\right)}}{(2\pi)^{N_s} \sqrt{|\det(\mathbf{\Gamma}_w)| \cdot |\det(\mathbf{\Gamma})|}}, \tag{25}$$

where z and l are expressed above. The correlation matrices $\mathbf{\Gamma}_w$ and $\mathbf{\Gamma}$ can be considered as *a-priori* known by the detector (at least in estimation). Based on the joint observation of amplitude and phase of the received signal vector, the ML decision rule can be expressed as

$$\begin{aligned} \hat{\underline{\mathbf{s}}} &= \underset{\underline{\mathbf{s}} \in \mathcal{C}'}{\arg\max} \quad p(\underline{\mathbf{r}} \mid \underline{\mathbf{s}}) \\ &= \underset{\underline{\mathbf{s}} \in \mathcal{C}'}{\arg\max} \quad \ln(p(\underline{\mathbf{r}} \mid \underline{\mathbf{s}})) \\ &= \underset{\underline{\mathbf{s}} \in \mathcal{C}'}{\arg\min} \, (\underline{\mathbf{r}}_\rho - \underline{\mathbf{s}}_\rho)^T \mathfrak{Re}\{\mathbf{\Gamma}_w\}^{-1}(\underline{\mathbf{r}}_\rho - \underline{\mathbf{s}}_\rho) + (\underline{\mathbf{r}}_\theta - \underline{\mathbf{s}}_\theta)^T \mathbf{\Gamma}^{-1}(\underline{\mathbf{r}}_\theta - \underline{\mathbf{s}}_\theta) + \log\left(|\det(\mathbf{\Gamma})|\right), \end{aligned} \tag{26}$$

where the estimated vector $\hat{\underline{\mathbf{s}}}$ is supposed to be the transmitted symbols sequence. It means that for DFT-s-OFDM systems in presence of a GPN, the ML decision rule involves the symbols transmitted over all the N_s subcarriers. The set $\mathcal{C}'$ thus contains all the possible transmitted sequences with a size of $(N_s)^{M_s}$, where M_s is the modulation order. For practical values, such as a FFT with 128 subcarriers and 16-QAM, i.e., $N_s = 128$ and $M_s = 16$, one realizes that the number of possibilities is far too large to perform the ML expression in (26) and thus, the decision rule cannot be implemented in practice. This severe complexity comes from the ICI correlated nature. That is why we propose to investigate a sub-optimal decision rule assuming that the ICI follows an uncorrelated Gaussian random process.

3.1.3 Sub-optimal detection criterion

For the sub-optimal detection, let us suppose that the ICI follows an uncorrelated complex Gaussian random process. This means that its correlation matrix is a diagonal matrix and we can defined it as follows

$$\gamma_k \frown \mathbb{CN}(m_{\gamma_k}, \sigma_{\gamma_k}^2) = \begin{cases} m_{\gamma_k} = 0 \\ \sigma_{\gamma_k}^2 = \mathbf{diag}_k\{\mathbf{\Gamma}_{\gamma}\}, \end{cases} \tag{27}$$

where m_{γ_k} and $\sigma_{\gamma_k}^2$ are, respectively, the mean and the variance of $\mathbf{\gamma}_k$. The expression (12) becomes

$$r_k \simeq s_k \cdot e^{j\Phi_k} + w_k, \tag{28}$$

where $\Phi_k \frown \mathcal{N}(0, \sigma_{\Phi_k}^2)$ and $w_k = \eta_k + \gamma_k$ is defined as follows

$$w_k \frown \mathbb{CN}(m_{w_k}, \sigma_{w_k}^2) = \begin{cases} m_{w_k} = m_{\eta_k} + m_{\gamma_k} \simeq 0 \\ \sigma_{w_k}^2 = \sigma_n^2 + \sigma_{\gamma_k}^2. \end{cases} \tag{29}$$

By considering the high SINR approximation, i.e., $\mathfrak{Re}\{w_k'\}$ and $\mathfrak{Im}\{w_k'\}$ almost 0; and $\arctan(x) = x$ if x small (see "Appendix 1"), the expressions (19) and (20) respectively become

$$\begin{aligned} r_{k_\rho} &= \left| (s_{k_\rho} + w_k') \cdot e^{j(\Phi_k + s_{k_\theta})} \right| \\ &\simeq s_{k_\rho} + \mathfrak{Re}\{w_k'\} \end{aligned} \tag{30}$$

$$\begin{aligned} r_{k_\theta} &= \arg\left((s_{k_\rho} + w_k') \cdot e^{j(\Phi_k + s_{k_\rho})} \right) \\ &\simeq s_{k_\theta} + \Phi_k + \frac{\mathfrak{Im}\{w_k'\}}{s_{k_\rho}}, \end{aligned} \tag{31}$$

where $w_k' = w_k \cdot e^{-j(\Phi_k + s_{k_\theta})} \frown \mathbb{CN}(0, \sigma_{w_k}^2)$. So, (21) can be simplified as follows

$$\begin{cases} r_{k_\rho} - s_{k_\rho} \frown \mathcal{N}(0, \sigma_{w_k}^2/2) \\ r_{k_\theta} - s_{k_\theta} \frown \mathcal{N}(0, \sigma_{\Phi_k}^2 + \frac{\sigma_{w_k}^2}{2s_{k_\rho}^2}). \end{cases} \tag{32}$$

The joint PDF of expressions in (32) is expressed as follows

$$p(r_k \mid s_k) = \frac{\exp\left(-\frac{1}{2}\left(\frac{(r_{k_\rho} - s_{k_\rho})^2}{\sigma_{w_k}^2/2} + \frac{(r_{k_\theta} - s_{k_\theta})^2}{\sigma_{\Phi_k}^2 + \sigma_{w_k}^2/2s_{k_\rho}^2}\right)\right)}{2\pi\sqrt{\frac{\sigma_{w_k}^2}{2}(\sigma_{\Phi_k}^2 + \sigma_{w_k}^2/2s_{k_\rho}^2)}}. \tag{33}$$

Hence, the ML decision rule using the channel likelihood expression (33) can be expressed as

$$\hat{s}_k = \underset{s_i \in \mathcal{C}}{\mathrm{argmax}} \; p(r \mid s_i)$$

$$= \underset{s_i \in \mathcal{C}}{\mathrm{argmax}} \; \ln(p(r \mid s_i))$$

$$= \underset{s_i \in \mathcal{C}}{\mathrm{argmin}} \; \frac{(r_{k_\rho} - s_{i_\rho})^2}{\sigma_{w_k}^2/2} + \frac{(r_{k_\theta} - s_{i_\theta})^2}{\sigma_{\Phi_k}^2 + \frac{\sigma_{w_k}^2}{2s_{i_\rho}^2}} + \log\left(\sigma_{\Phi_k}^2 + \frac{\sigma_{w_k}^2}{2s_{i_\rho}^2}\right). \tag{34}$$

Contrary to what was presented earlier, the ML decision rule independently involves each subcarrier k. The number of possibilities is reduced to the size of the constellation just like for the conventional Euclidean decision rule. The proposed polar detector based on the ML metric (34) will be denoted by *SUB-D* from now.

3.1.4 Estimation of the required a-priori knowledge

The challenge in applying this detector relies in estimating $\sigma_{\Phi_k}^2$ and $\sigma_{\gamma_k}^2$ in realistic transmission scenarios. Let us first focus on the estimation of $\sigma_{\Phi_k}^2$. The main idea is to express the relation between the phase error at the signal level $e^{j\underline{\boldsymbol{\Phi}}}$ and the phase error at the oscillator level $e^{j\underline{\boldsymbol{\phi}}}$

$$e^{j\underline{\boldsymbol{\Phi}}} = \mathbf{B} e^{j\underline{\boldsymbol{\phi}}} \quad \text{with} \quad \mathbf{B}^{(i,k)} = \mathbf{A}_{RX}^{(i,k)} \mathbf{A}_{TX}^{(k,i)}, \tag{35}$$

for $i \in [\![0, \cdots, N_s - 1]\!]$ and $k \in [\![0, \cdots, N_f - 1]\!]$. The matrices $\mathbf{A}_{TX}$ and $\mathbf{A}_{RX}$ are defined as follows

$$\mathbf{A}_{TX} = \mathbf{F}_{N_f}^H \mathbf{M}_{TX} \mathbf{F}_{N_s} \quad \text{and} \quad \mathbf{A}_{RX} = \mathbf{F}_{N_s}^H \mathbf{D}_{RX} \mathbf{F}_{N_f}, \tag{36}$$

where $\mathbf{M}_{TX}$ and $\mathbf{D}_{RX}$ respectively represent the N_s-to-N_f mapping matrix and the N_f-to-N_s demapping matrix. By using the small angle approximation, the expression (35) gives

$$\underline{\mathbf{1}}_{N_s} + j\underline{\boldsymbol{\Phi}} = \mathbf{B}\left(\underline{\mathbf{1}}_{N_f} + j\underline{\boldsymbol{\phi}}\right) \iff \underline{\boldsymbol{\Phi}} = \mathbf{B}\underline{\boldsymbol{\phi}}, \tag{37}$$

because $\mathbf{B} \in \mathbb{R}^{N_s \times N_f}$. Then, the correlation matrix of $\underline{\boldsymbol{\Phi}}$, $\mathbf{R}_{\underline{\boldsymbol{\Phi}}} = \mathbb{E}\left[\underline{\boldsymbol{\Phi}} \cdot \underline{\boldsymbol{\Phi}}^H\right]$, can be expressed as function of the correlation matrix $\mathbf{R}_{\underline{\boldsymbol{\phi}}}$ of the PN $\underline{\boldsymbol{\phi}}$ as bellow

$$\mathbf{R}_{\underline{\boldsymbol{\Phi}}} = \mathbf{B}\mathbf{R}_{\underline{\boldsymbol{\phi}}}\mathbf{B}^H \cdot \tag{38}$$

Consequently, we compute the expression (14) upon (38) to obtain the different $\sigma_{\Phi_k}^2$ for each DFT subcarrier k as follows

$$\sigma_{\Phi_k}^2 = \mathbf{diag}_k\{\mathbf{B}\mathbf{R}_{\underline{\boldsymbol{\phi}}}\mathbf{B}^H\}. \tag{39}$$

The expression (39) states that it is possible to evaluate the variance of the SPE, $\sigma_{\Phi_k}^2$, directly from the stochastic model of the local oscillators $\mathbf{R}_{\underline{\boldsymbol{\phi}}}$. Therefore, if one samples the response of a intermediate-frequency oscillator and measures the variance of the phase jitter, they can determine the variance of the SPE [41].

Regarding the demonstration presented in "Appendix 2", the ICI power is defined for $k \in [\![0, \cdots, N_s - 1]\!]$ by the following relation
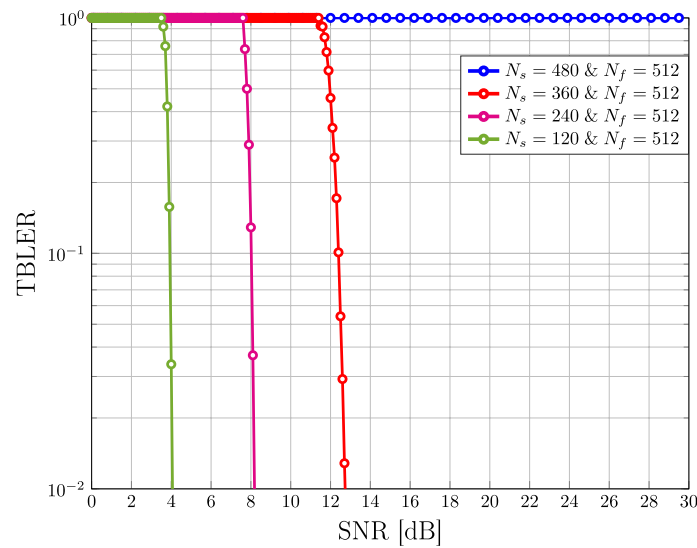
Fig. 8 DFT-s-OFDM with *EUC-D*, 16-QAM, LDPC CR= 0.7 for configurations defined in Table 3

$$\sigma_{\gamma_k}^2 \simeq \sigma_\phi^2 - \sigma_{\Phi_k}^2. \tag{40}$$

We already know that the Local Oscillator (LO)-induced PN results in a random rotation and the generation of ICI after Fourier transformations. However, (40) goes further and states that the variance of the LO Phase error σ_ϕ^2 corresponds to the sum of the variance of the SPE $\sigma_{\Phi_k}^2$ and the power of the ICI $\sigma_{\gamma_k}^2$. As a consequence, when a subcarrier k suffers from strong ICI, the SPE is limited and conversely. In addition, because we know that the SPE is frequency-dependent, it proves that for a DFT-s-OFDM waveform, some subcarriers are dominated by the rotation effects while other by the presence of ICI.

3.2 Performance evaluation

In this section, we evaluate the performance of following systems under GPN channels:

- OFDM with Euclidean detector (*EUC-D*)
- DFT-s-OFDM with Euclidean detector (*EUC-D*)
- DFT-s-OFDM with the proposed sub-optimal polar detector (*SUB-D*)

The Euclidean detector *EUC-D* correspond to the ML detection defined by

$$\hat{s}_k = \underset{s_i \in \mathcal{C}}{\operatorname{argmin}} \ \| r_k - s_i \|_2^2, \tag{41}$$

where symbols $s_i \in \mathcal{C}$, with $\mathcal{C}$ the set of the selected modulation scheme. The sub-optimal polar detector (*SUB-D*) applies the decision rule expressed in (34). The latter detection criterion is only evaluated with DFT-s-OFDM signals as it is directly derived from DFT-s-OFDM baseband model. The performance of DFT-s-OFDM with *SUB-D* will be assessed first in Genie-aided conditions and then in realistic conditions (i.e., with estimation of unknown variances as detailed in Sect. 3.1.4). The performance indicator is the Transport Block Error Rate (TBLER) as a function of the Signal-to-Noise Ratio
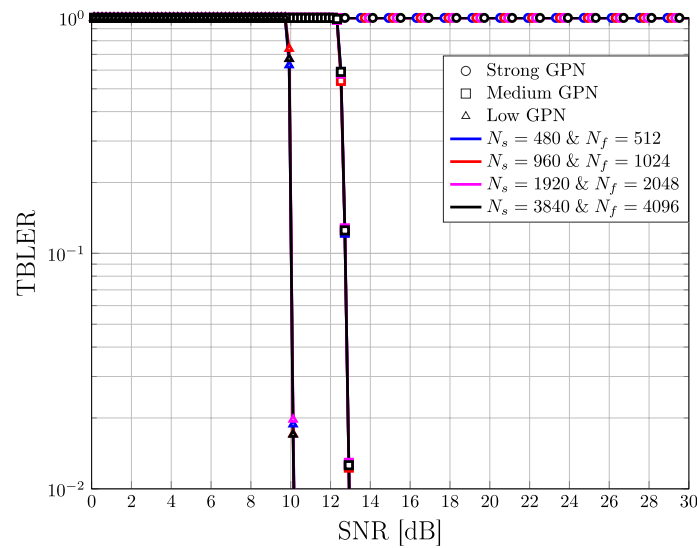
Fig. 9 DFT-s-OFDM with *EUC-D*, 16-QAM, LDPC CR= 0.7 for configurations defined in Table 4

(SNR) while considering a 16-QAM modulation and a low density parity check (LDPC) following the 5G-NR specifications [44] with a code rate (CR) equal to 0.7.

3.2.1 Impact of DFT parameters

As we mentioned in this paper, DFT-s-OFDM operates as a compromise between SC and OFDM systems depending on the value of the ratio ζ. Therefore, we propose in a first time to observe the achieved performance of DFT-s-OFDM systems with configurations defined in Table 3 (i.e., by varying ζ) and in Table 4 (i.e., with constant ζ) for the conventional *EUC-D* detector. The results are, respectively, depicted in Figs. 8 and 9.

From Fig. 8, one can notice that reducing the DFT spreading size N_s allows to reach the targeted TBLER of 10^{-2} with a low SNR. Indeed, enlarging the useful system bandwidth B_W (by increasing N_s) integrates more GPN power and thus degrades the signal quality. That is why for higher values of N_s, higher SNR are required to successfully decode the signal or not (if the GPN power is very high). Then for a fixed system bandwidth, there is no performance penalty for numerologies from 6 to 9 as one can observe by looking at Fig. 9. Therefore, enlarging the ICS does not help and DFT-s-OFDM with the *EUC-D* decision rule does not work under strong GPN regime.

3.2.2 Comparison of detection techniques

The results presented above demonstrate the inefficiency of the Euclidean detector when the PN power is high (larger ζ). In this section, we compare our proposed detector *SUB-D* with the Euclidean detector *EUC-D*. We compare both DFT-s-OFDM and OFDM assuming the same bandwidth, i.e., by considering N_s active subcarriers among the N_f for the OFDM modulation.

Figure 10 shows the system performance for the different GPN regimes and genie-aided *SUB-D* detector. In strong GPN regime, one can first observe that the two *EUC-D* receivers do not perform well as they cannot achieve a TBLER $< 10^{-1}$ with SNR $= 30$
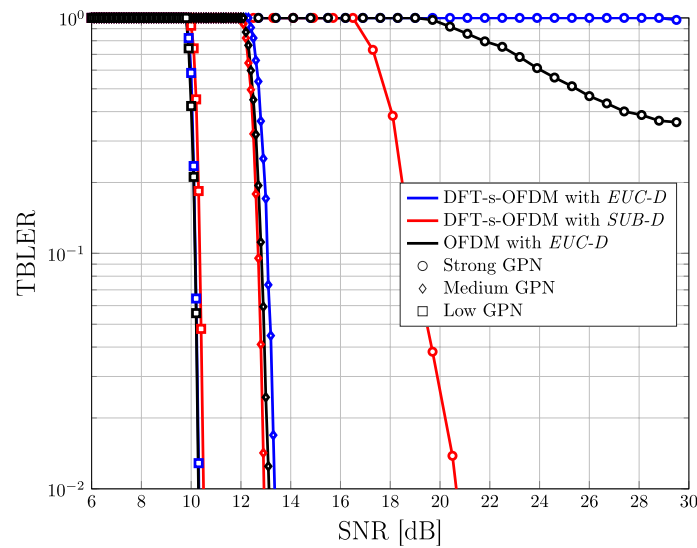
Fig. 10 Comparison of achieved performance for the three GPN regimes, 16-QAM, LDPC with CR=0.7 and $N_s = 480, N_f = 512$ ($\zeta = 0.9375$ for DFT-s-OFDM)
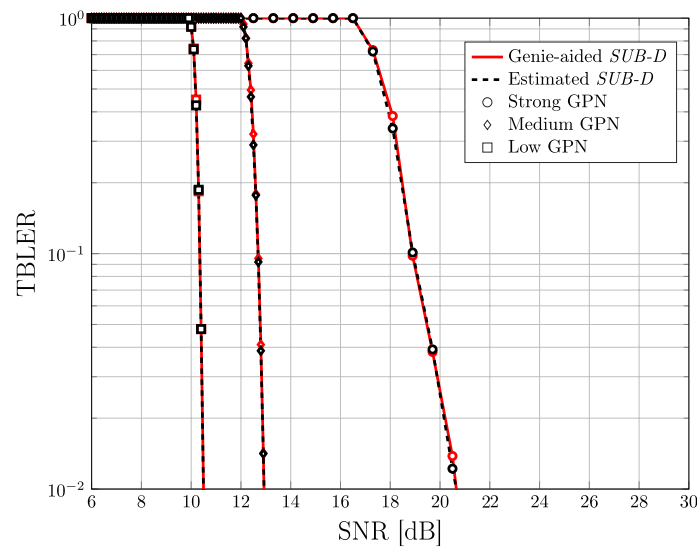

Fig. 11 Comparison of achieved performance with genie-aided and realistic DFT-s-OFDM *SUB-D* system for the three GPN regimes, 16-QAM, LDPC with CR=0.7 and $\zeta = 0.9375$ ($N_s = 480, N_f = 512$)

dB. Fortunately, the proposed DFT-s-OFDM with *SUB-D* receiver succeeds in decoding packets and can even reach a TBLER of 10^{-2} for SNR $\simeq$ 21 dB. In medium GPN regime, our proposed detector still outperforms the *EUC-D* but with a small SNR gain compared to the strong GPN case. For low GPN, the *EUC-D* detector has almost the same performance as the *SUB-D*, but it is slightly better than the *SUB-D*.

We have demonstrated the gain of the *SUB-D* detector over the *EUC-D* detector in a strong GPN regime and genie-aided conditions (perfect knowledge of SPE and ICI stochastic properties). Indeed, the polar detection criterion makes sense when phase distortion is dominant. As a consequence, DFT-s-OFDM with the proposed *SUB-D* detector is an enabler for communications under strong GPN regime. As a
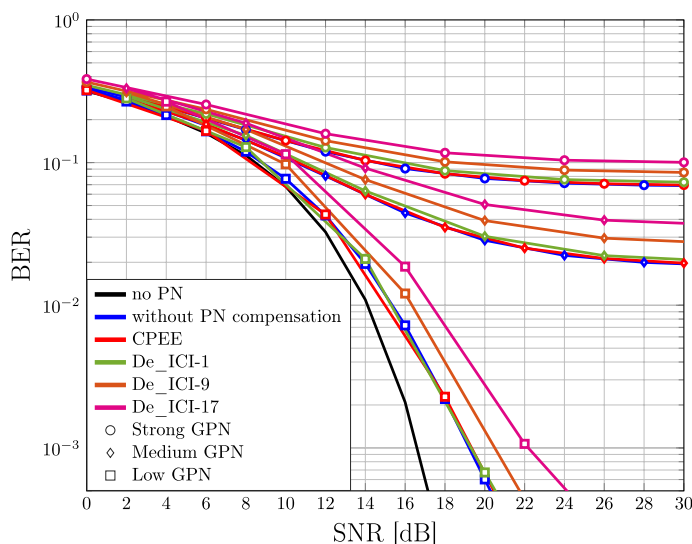
Fig. 12 OFDM performance: raw BER in function of the SNR, 16-QAM, FFT size of 512 with 480 active subcarriers and 3.686-GHz bandwidth

consequence, for the considered scenarios, the assumption of independent ICI is sufficiently valid.

Figure 11 presents and compares the performance achieved by the genie-aided and the realistic DFT-s-OFDM/*SUB-D* receiver, i.e., by considering the expressions (39) and (40). One can notice the estimated *SUB-D* yields the same results as the genie-aided one. These results validate the proposed estimation approach.

4 Discussions

ICI cancellation techniques have also been investigated, especially for OFDM systems [17, 19]. In those studies, PN is generally assumed partially correlated [24]. We decide to evaluate the performance of the commonly used De_ICI algorithm [17] under GPN channel. The results are depicted in Fig. 12. The De_ICI algorithm means filtering the OFDM received signal in the frequency domain (post-FFT domain) with a filter of length L_f. In [17], the authors show that the increase of L_f enhances the mitigation of the ICI at the price of increased complexity. In what follows, De_ICI-L_f denotes the application of the De_ICI technique with a filter of length L_f. For comparison, the case without PN (ideal scenario), with GPN but without any compensation techniques and with GPN and CPE Estimation (CPEE) algorithm [15] are presented. The CPEE algorithm compensates the common phase error (i.e., the constellation rotation) of the received signal (no ICI mitigation). The De_ICI-1 is equivalent to the CPE compensation [17].

In Fig. 12, the uncoded bit error rate (BER) is evaluated as function of the SNR under GPN channel. First, one can notice that the CPEE algorithm does not provide any performance gain with respect to uncompensated case. This result is expected because GPN is a zero-mean phase error noise, therefore the CPE tends to zero with probability 1 (meaning that with GPN there is only a negligible symbol rotation for OFDM constellations). CPEE algorithm is only beneficial when correlated PN are involved. When it comes to the De_ICI, the algorithm fails at mitigating the ICI power even for filter lengths up to $N_f = 17$.

Indeed, with GPN the correlated nature of the ICI is limited, as we observed with DFT-s-OFDM in this article and therefore, the De_ICI does not successfully remove the ICI from the received signal. It implies that, for OFDM systems, GPN leads to the generation of ICI (and no CPE), whereas with DFT-s-OFDM, it leads to both a random rotation and generation of ICI. The power of the resulting ICI in DFT-s-OFDM is thus lower than for OFDM. It allows to adapt the decision rule as presented in this article which results in significant performance gain especially when strong GPN regime is involved. That is the reason why DFT-s-OFDM is more suited than OFDM for transmissions under strong GPN channels.

5 Conclusion

In this paper, we investigated the effects of GPN on OFDM and DFT-s-OFDM waveforms. In DFT-s-OFDM systems, the presence of GPN results in two distortions i) a frequency-dependent random rotation of the received constellation named SPE and ii) the generation of additive ICI. Their random distributions have been characterized. It appears that, in DFT-s-OFDM, the random rotation dominates against the generation of ICI for some subcarriers and conversely. That is why we studied and derived the optimal decision rule to be applied on each subcarrier. This optimal decision rule is too complex to be implemented in practical devices, thus, we derived a sub-optimal detector and compared its achievable performance with the conventional Euclidean-distance-based criterion. We can draw two conclusions from the obtained results: i) known PN mitigation techniques designed when the PN exhibits a partially correlated nature (especially for MC systems) prove to be inefficient under GPN channels and, ii) DFT-s-OFDM with the proposed polar detector significantly outperforms its OFDM contender when strong GPN regimes are involved. That is the reason why we believe that DFT-s-OFDM is a promising enabler of sub-THz transmissions under strong GPN channels.

Nonetheless, all the work presented above is based on the assumption that the channel is dominated by its LoS contribution. Even if this assumption has been validated by recent studies [46–49], some scenarios with a second strong resolvable path can exist such as indoor environment, vehicular communications with the ground rebound. In such cases, our work cannot be trivially extended because the propagation channels become frequency selective. Furthermore, when the PN has an uncorrelated nature, it could interfere with tracking and channel estimation in real time. Joint channel estimation and GPN-induced impairments must be considered which is one interesting study perspective of the presented work.

Appendix 1: High SINR approximation

The Symbol Error Probability is minimized by the Maximum Likelihood (ML) decision criterion for equi-probable and independent symbols. The channel likelihood function can be written as follows [29, 30]:

$$p(\underline{\mathbf{r}}|\underline{\mathbf{s}}) = p(\underline{\mathbf{r}}_\rho, \underline{\mathbf{r}}_\theta \mid \underline{\mathbf{s}}_\rho, \underline{\mathbf{s}}_\theta) \cdot \tag{42}$$

Thus, we have to express more clearly the ML decision criterion. Before studying the amplitude and phase of the received signal vector $\underline{\mathbf{r}}$, we denote $\underline{\mathbf{w}} \odot e^{-j(\underline{\boldsymbol{\Phi}} + \underline{\mathbf{s}}_\theta)}$ by $\underline{\mathbf{w}}'$. The post-FFT noise $\underline{\mathbf{w}}'$ has the same stochastic properties as the additive channel noise $\underline{\mathbf{w}}$

Bello *et al. J Wireless Com Network*   (2024) 2024:60

Page 24 of 29

(i.e., zero-mean circular symmetric complex Gaussian noise). The amplitude and phase of the received DFT-s-OFDM symbol is, respectively, given by (43) and (44).

$$
\begin{aligned}
\underline{\mathbf{r}}_\rho[k] &= \sqrt{(\underline{\mathbf{s}}_\rho[k] + \mathfrak{Re}\{\underline{\mathbf{w}}'[k]\})^2 + \mathfrak{Im}\{\underline{\mathbf{w}}'[k]\}^2}\,, \\
&= (\underline{\mathbf{s}}_\rho[k] + \mathfrak{Re}\{\underline{\mathbf{w}}'[k]\})\sqrt{1 + \left(\frac{\mathfrak{Im}\{\underline{\mathbf{w}}'[k]\}}{(\underline{\mathbf{s}}_\rho[k] + \mathfrak{Re}\{\underline{\mathbf{w}}'[k]\})}\right)^2}
\end{aligned}
\tag{43}
$$

$$
\begin{aligned}
\underline{\mathbf{r}}_\theta[k] &= \arg\left((\underline{\mathbf{s}}_\rho[k] + \underline{\mathbf{w}}'[k]) \odot e^{j(\mathbf{\Phi}[k] + \underline{\mathbf{s}}_\theta[k])}\right) \\
&= \underline{\mathbf{s}}_\theta[k] + \underline{\mathbf{\Phi}}[k] + \arctan\left(\frac{\mathfrak{Im}\{\underline{\mathbf{w}}'[k]\}}{\underline{\mathbf{s}}_\rho[k] + \mathfrak{Re}\{\underline{\mathbf{w}}'[k]\}}\right)
\end{aligned}
\tag{44}
$$

One can express $\underline{\mathbf{w}}'[k]$ in its polar form by setting $\underline{\mathbf{w}}'[k] = \rho_w[k]e^{j\Phi_w[k]}$. The high SNR approximation means that the noise power becomes negligible with respect to the signal power, i.e., $\rho_w[k]/\underline{\mathbf{s}}_\rho[k] \to 0$. By applying this approximation on (43) and (44), one obtains

$$
\lim_{\rho_w[k]/\underline{\mathbf{s}}_\rho[k] \to 0} \frac{\mathfrak{Im}\{\underline{\mathbf{w}}'[k]\}}{\underline{\mathbf{s}}_\rho[k] + \mathfrak{Re}\{\underline{\mathbf{w}}'[k]\}} = \lim_{\rho_w[k]/\underline{\mathbf{s}}_\rho[k] \to 0} \frac{\rho_w[k]\sin(\Phi_w[k])}{\underline{\mathbf{s}}_\rho[k] + \rho_w[k]\cos(\Phi_w[k])}
$$
$$
= 0
\tag{45}
$$

and

$$
\lim_{\rho_w[k]/\underline{\mathbf{s}}_\rho[k] \to 0} \left(\underline{\mathbf{s}}_\rho[k] + \mathfrak{Re}\{\underline{\mathbf{w}}'[k]\}\right) = \lim_{\rho_w[k]/\underline{\mathbf{s}}_\rho[k] \to 0} \left(\underline{\mathbf{s}}_\rho[k] + \rho_w[k]\cos(\Phi_w[k])\right)
$$
$$
= \underline{\mathbf{s}}_\rho[k]\,.
\tag{46}
$$

It eventually leads to:

$$
\begin{aligned}
\underline{\mathbf{r}}_\rho[k] &= \sqrt{(\underline{\mathbf{s}}_\rho[k] + \mathfrak{Re}\{\underline{\mathbf{w}}'[k]\})^2 + \mathfrak{Im}\{\underline{\mathbf{w}}'[k]\}^2} \\
&\approx \underline{\mathbf{s}}_\rho[k] + \mathfrak{Re}\{\underline{\mathbf{w}}'[k]\}
\end{aligned}
\tag{47}
$$

and

$$
\begin{aligned}
\underline{\mathbf{r}}_\theta[k] &= \underline{\mathbf{s}}_\theta[k] + \underline{\mathbf{\Phi}}[k] + \arctan\left(\frac{\mathfrak{Im}\{\underline{\mathbf{w}}'[k]\}}{\underline{\mathbf{s}}_\rho[k] + \mathfrak{Re}\{\underline{\mathbf{w}}'[k]\}}\right) \\
&\approx \underline{\mathbf{s}}_\theta[k] + \underline{\mathbf{\Phi}}[k] + \frac{\mathfrak{Im}\{\underline{\mathbf{w}}'[k]\}}{\underline{\mathbf{s}}_\rho[k] + \mathfrak{Re}\{\underline{\mathbf{w}}'[k]\}}
\end{aligned}
\tag{48}
$$

$$
\approx \underline{\mathbf{s}}_\theta[k] + \underline{\mathbf{\Phi}}[k] + \frac{\mathfrak{Im}\{\underline{\mathbf{w}}'[k]\}}{\underline{\mathbf{s}}_\rho[k]}\,.
\tag{49}
$$

Thus, we obtain

$$\begin{cases} \underline{\mathbf{r}}_\rho - \underline{\mathbf{s}}_\rho \simeq \mathfrak{Re}\{\underline{\mathbf{w}}'\} \\ \underline{\mathbf{r}}_\theta - \underline{\mathbf{s}}_\theta \simeq \underline{\mathbf{\Phi}} + \mathfrak{Im}\{\underline{\mathbf{w}}'\} \odot \underline{\mathbf{s}}_\rho^{-1}. \end{cases} \tag{50}$$

Appendix 2: Relation between ICI power and variance of the SPE

Let us consider $\underline{\mathbf{s}}$ as the data symbol vector before the DFT transformation at the transmitter. The expression of the received signal $\underline{\mathbf{r}}$ after Fourier transformations can be expressed by

$$\underline{\mathbf{r}} = \underbrace{\mathbf{F}_{N_s}^H \mathbf{D}_{RX} \mathbf{F}_{N_f}}_{\mathbf{A}_{RX}} \mathbf{Q} \underbrace{\mathbf{F}_{N_f}^H \mathbf{M}_{TX} \mathbf{F}_{N_s}}_{\mathbf{A}_{TX}} \underline{\mathbf{s}} = \mathbf{C}\underline{\mathbf{s}}, \tag{51}$$

where $\mathbf{C} = \mathbf{A}_{RX}\mathbf{Q}\mathbf{A}_{TX}$. The terms $\mathbf{F}_{N_s}$ and $\mathbf{F}_{N_f}$ respectively are the Fourier transform matrix of size N_s and N_f. The matrices $\mathbf{M}_{TX}$ and $\mathbf{D}_{RX}$ respectively represent the N_s-to-N_f mapping and N_f-to-N_s demapping. The matrix $\mathbf{Q}$ is a diagonal matrix such that $\mathbf{diag}\{\mathbf{Q}\} = e^{j\underline{\boldsymbol{\phi}}}$, where $\underline{\boldsymbol{\phi}}$ represents the GPN generated by the oscillators at transmitter and receiver side. We can develop the expression (51) as follows

$$\begin{aligned} \underline{\mathbf{r}} &= \mathbf{G}\underline{\mathbf{s}} + \mathbf{K}\underline{\mathbf{s}} \\ &= \underline{\mathbf{s}} \odot \underline{\boldsymbol{\beta}} + \underline{\boldsymbol{\gamma}} \end{aligned} \tag{52}$$

where $\underline{\boldsymbol{\beta}}$ is the SPE vector and $\underline{\boldsymbol{\gamma}}$ the ICI vector. The term $\mathbf{G}$ represents a diagonal matrix such that

$$\mathbf{diag}\{\mathbf{G}\} = \mathbf{diag}\{\mathbf{C}\} = \underline{\boldsymbol{\beta}}, \tag{53}$$

and $\mathbf{K} = \mathbf{C} - \mathbf{G}$, where $\mathbf{K}$ is the ICI matrix. The expression of the ICI correlation matrix is given by

$$\begin{aligned} \mathbf{R_K} &= \mathbb{E}\big[\mathbf{KK}^H\big] = \mathbb{E}\big[(\mathbf{C} - \mathbf{G})(\mathbf{C} - \mathbf{G})^H\big] \\ &= \mathbb{E}\big[\mathbf{CC}^H - \mathbf{CG}^H - \mathbf{GC}^H + \mathbf{GG}^H\big] \\ &= \mathbb{E}\big[\mathbf{CC}^H - (\mathbf{CG}^H + \mathbf{GC}^H) + \mathbf{GG}^H\big]. \end{aligned} \tag{54}$$

The second term of (54) in bracket can be simplified as follows

$$\begin{aligned} \mathbf{CG}^H + \mathbf{GC}^H &= (\mathbf{GG}^H + \mathbf{KG}^H) + (\mathbf{GG}^H + \mathbf{GK}^H) \\ &= 2\mathbf{GG}^H + \mathbf{0}_{N_s}, \end{aligned} \tag{55}$$

by realizing that $\mathbf{GK}^H = \mathbf{0}_{N_s}$ is the product of a diagonal matrix $\mathbf{G}$ with a zero diagonal elements matrix $\mathbf{K}$ (similarly $\mathbf{KG}^H = \mathbf{0}_{N_s}$). By combining (55) and (54), one obtains

$$\begin{aligned} \mathbf{R_K} &= \mathbb{E}\big[\mathbf{CC}^H - \mathbf{GG}^H\big] \\ &= \mathbb{E}\big[\mathbf{CC}^H\big] - \mathbb{E}\big[\mathbf{GG}^H\big] \\ &= \mathbf{A}_{RX}\mathbb{E}\big[\mathbf{QQ}^H\big]\mathbf{A}_{RX}^H - \mathbb{E}\big[\mathbf{GG}^H\big]. \end{aligned} \tag{56}$$

Let's simplify the expressions of $\mathbb{E}\big[\mathbf{QQ}^H\big]$ and $\mathbb{E}\big[\mathbf{GG}^H\big]$. We have

$$\mathbb{E}\left[\mathbf{Q}\mathbf{Q}^{H}\right] = \mathbb{E}\left[\mathbf{diag}\left\{e^{j\underline{\phi}}\left(e^{j\underline{\phi}}\right)^{H}\right\}\right] \text{ because } \mathbf{diag}\{\mathbf{Q}\} = e^{j\underline{\phi}}$$

$$= \mathbf{diag}\left\{\mathbb{E}\left[e^{j\underline{\phi}}\left(e^{j\underline{\phi}}\right)^{H}\right]\right\}$$

$$= \mathbf{diag}\left\{\mathbf{R}_{e^{\underline{\phi}}}\right\} \cdot \mathbf{I}_{N_f}. \tag{57}$$

The small angle approximation [41] leads to

$$\mathbb{E}\left[\mathbf{Q}\mathbf{Q}^{H}\right] \simeq \mathbf{diag}\left\{\mathbf{1}_{N_f} + \mathbf{R}_{\underline{\phi}}\right\} \cdot \mathbf{I}_{N_f}$$

$$\simeq \left(1 + \sigma_{\phi}^{2}\right) \cdot \mathbf{I}_{N_f}, \tag{58}$$

because $\mathbf{R}_{\underline{\phi}} = \sigma_{\phi}^{2} \cdot \mathbf{I}_{N_f}$. Now, we will derive the second expectation term $\mathbb{E}\left[\mathbf{G}\mathbf{G}^{H}\right]$ as bellow

$$\mathbb{E}\left[\mathbf{G}\mathbf{G}^{H}\right] = \mathbb{E}\left[\mathbf{diag}\left\{\underline{\beta}\,\underline{\beta}^{H}\right\}\right], \text{ because } \mathbf{diag}\{\mathbf{G}\} = \underline{\beta}$$

$$= \mathbf{diag}\left\{\mathbb{E}\left[\underline{\beta}\,\underline{\beta}^{H}\right]\right\}$$

$$\simeq \mathbf{diag}\left\{\mathbf{R}_{e^{\underline{\Phi}}}\right\}, \text{ because } \underline{\beta} \simeq e^{\underline{\Phi}} \text{ based on results obtained in 2.2} \tag{59}$$

$$\simeq \mathbf{diag}\left\{\mathbf{1}_{N_s} + \mathbf{R}_{\underline{\Phi}}\right\}, \text{ based on the small angle approximation}$$

$$\simeq \mathbf{I}_{N_s} + \mathbf{diag}\left\{\mathbf{R}_{\underline{\Phi}}\right\}$$

$$\simeq \mathbf{I}_{N_s} + \mathbf{Z},$$

where $\mathbf{Z}$ is a diagonal matrix such that $\mathbf{diag}\{\mathbf{Z}\} = \mathbf{diag}\left\{\mathbf{R}_{\underline{\Phi}}\right\}$. Therefore, the expression (56) becomes

$$\mathbf{R}_{\mathbf{K}} \simeq \left(1 + \sigma_{\phi}^{2}\right) \cdot \mathbf{A}_{RX}\mathbf{A}_{RX}^{H} - \left(\mathbf{I}_{N_s} + \mathbf{Z}\right)$$

$$\simeq \left(1 + \sigma_{\phi}^{2}\right) \cdot \mathbf{I}_{N_s} - \left(\mathbf{I}_{N_s} + \mathbf{Z}\right). \tag{60}$$

Since we use normalized QAM schemes for data modulation, i.e., $\mathbb{E}\left[\underline{\mathbf{s}}\,\underline{\mathbf{s}}^{H}\right] = \mathbf{I}_{N_s}$, the correlation matrix of the ICI vector is given by

$$\mathbf{R}_{\underline{\gamma}} = \mathbb{E}\left[\underline{\gamma}\,\underline{\gamma}^{H}\right] = \mathbb{E}\left[\mathbf{K}\underline{\mathbf{s}}\,\underline{\mathbf{s}}^{H}\mathbf{K}^{H}\right]$$

$$= \mathbb{E}\left[\mathbf{K}\mathbf{K}^{H}\right] \tag{61}$$

$$= \mathbf{R}_{\mathbf{K}}.$$

Finally, the expression of the ICI power at a subcarrier k according to the expressions (27) and (60) is given by

$$\sigma_{\gamma_k}^{2} = \mathbf{diag}_{k}\{\mathbf{R}_{\mathbf{K}}\}$$

$$\simeq \mathbf{diag}_{k}\left\{\left(1 + \sigma_{\phi}^{2}\right) \cdot \mathbf{I}_{N_s}\right\} - \mathbf{diag}_{k}\left\{\left(\mathbf{I}_{N_s} + \mathbf{Z}\right)\right\}$$

$$\simeq 1 + \sigma_{\phi}^{2} - 1 - \mathbf{diag}_{k}\{\mathbf{Z}\} \tag{62}$$

$$\simeq \sigma_{\phi}^{2} - \mathbf{diag}_{k}\left\{\mathbf{R}_{\underline{\Phi}}\right\}.$$

Finally, since $\mathbf{R}_{\underline{\Phi}}$ is a diagonal matrix such that $\sigma_{\Phi_k}^{2} = \mathbf{diag}_{k}\left\{\mathbf{R}_{\underline{\Phi}}\right\}$, the ICI power at subcarrier k is

$$\sigma_{\gamma_k}^2 \simeq \sigma_\phi^2 - \sigma_{\Phi_k}^2, \tag{63}$$

where σ_ϕ^2 represents the GPN power generated by oscillators in (3) and $\sigma_{\Phi_k}^2$ the SPE power at subcarrier k.

Abbreviations

N_s	Size of the DFT spreading block
N_f	Size of the FFT block
μ	Numerology
B_W	System bandwidth
F_s	Sampling frequency
K_0	Power spectral density of the phase noise
5G-NR	5G new radio
BER	Bit error rate
CDF	Cumulative distribution function
CP	Cyclic Prefix
CPE	Common phase error
CR	Coding rate
DFT	Discrete Fourier transform
DFT-s-OFDM	DFT-spread-OFDM
FFT	Fast Fourier transform
GPN	Gaussian PN
ICI	Inter-carrier interference
ICS	Inter-carrier spacing
LoS	Line-of-sight
MC	Multi-carrier
ML	Maximum likelihood
OFDM	Orthogonal frequency division multiplexing
PAPR	Peak-to-average power ratio
PDF	Probability density function
PN	Phase noise
PSD	Power spectral density
PT-RS	Phase tracking reference signals
RF	Radio frequency
SC	Single-carrier
SINR	Signal-to-interference-plus-noise ratio
SNR	Signal-to-noise ratio
SPE	Subcarrier phase error
TBLER	Transport block error rate

Availability of data and materials
The datasets used and/or analyzed during the current study are available from the corresponding author on reasonable request.

Declarations

Competing interests
The authors declare that they have no conflict of interest.

References

1. V. Petrov, T. Kurner, I. Hosako, IEEE 802.15.3d: first standardization efforts for sub-terahertz band communications toward 6G. IEEE Commun. Mag. **58**(11), 28–33 (2020). https://doi.org/10.1109/MCOM.001.2000273
2. J.-B. Doré, Y. Corre, S. Bicais, J. Palicot, E. Faussurier, D. Kténas, F. Bader, Above-90GHz spectrum and single-carrier waveform as enablers for efficient Tbit/s wireless communications, in *Proceedings of International Conference on Telecommunications (ICT)*, Saint-Malo, France (2018)
3. 3GPP: NR; User Equipement (UE) radio transmission and reception; Part 1: Range 1 Standalone. Technical Specification (TS) 38.101-1, 3rd Generation Partnership Project (3GPP) (December 2023). Version 17.12.0
4. O. Tervo, T. Levanen, K. Pajukoski, J. Hulkkonen, P. Wainio, M. Valkama, 5G New Radio Evolution Towards Sub-THz Communications, in *Proceedings 2nd 6G wireless summit (6G SUMMIT)*, pp. 1–6 (2020). https://doi.org/10.1109/6GSUMMIT49458.2020.9083807
5. T. Pollet, M. Moeneclaey, Synchronizability of OFDM signals, in *Proceedings IEEE Global Communications Conference (GLOBECOM)*, vol. 3, pp. 2054–20583 (1995). https://doi.org/10.1109/GLOCOM.1995.502767
6. M.V. Clark, Adaptive frequency-domain equalization and diversity combining for broadband wireless communications. IEEE J. Sel. Areas Commun. **16**(8), 1385–1395 (1998). https://doi.org/10.1109/49.730448
7. N. Dinur, D. Wulich, Peak to average power ratio in amplitude clipped high order OFDM, in *Proceedings of IEEE Military Communications Conference (MILCOM)* (Cat. No.98CH36201), vol. 2, pp. 684–6872 (1998). https://doi.org/10.1109/MILCOM.1998.722213
8. T. Oskari, N. Ilmari, N.I. Peruga, T. Esa, H. Jari, On the potential of using sub-THz frequencies for beyond 5G, in *Joint European Conference on Networks and Communications & 6G Summit (EuCNC/6G Summit)*, pp. 37–42 (2022). https://doi.org/10.1109/EuCNC/6GSummit54941.2022.9815761
9. G. Berardinelli, K.I. Pedersen, T.B. Sorensen, P. Mogensen, Generalized DFT-spread-OFDM as 5G waveform. IEEE Commun. Mag. **54**(11), 99–105 (2016). https://doi.org/10.1109/MCOM.2016.1600313CM
10. S. Merchan, A.G. Armada, J.L. Garcia, OFDM performance in amplifier nonlinearity. IEEE Trans. Broadcast. **44**(1), 106–114 (1998). https://doi.org/10.1109/11.713060
11. A. Demir, Computing timing jitter from phase noise spectra for oscillators and phase-locked loops with white and $1/f$ noise. IEEE Trans. Circuits Syst. I Regular Papers **53**(9), 1869–1884 (2006). https://doi.org/10.1109/TCSI.2006.881184
12. T. Pollet, M. Van Bladel, M. Moeneclaey, BER sensitivity of OFDM systems to carrier frequency offset and Wiener phase noise. IEEE Trans. Commun. **43**(2/3/4), 191–193 (1995). https://doi.org/10.1109/26.380034
13. A. Garcia Armada, Understanding the effects of phase noise in orthogonal frequency division multiplexing (OFDM). IEEE Trans. Broadcast. **47**(2), 153–159 (2001). https://doi.org/10.1109/11.948268
14. D. Petrovic, W. Rave, G. Fettweis, Intercarrier interference due to phase noise in OFDM - estimation and suppression, in *Proceedings of IEEE 60th Vehicular Technology Conference (VTC-Fall)*, vol. 3, pp. 2191–2195 (2004). https://doi.org/10.1109/VETECF.2004.1400429
15. J.-C. Sibel, Pilot-based phase noise tracking for uplink DFT-s-OFDM in 5G, in *Proceeding International Conference Telecommunications (ICT)*, pp. 52–56 (2018). https://doi.org/10.1109/ICT.2018.8464891
16. Y. Qi, M. Hunukumbure, H. Nam, H. Yoo, S. Amuru, On the phase tracking reference signal (PT-RS) design for 5G new radio (NR), in *Proceedings of IEEE Vehicular Technology Conference (VTC-Fall)* (2018). https://doi.org/10.1109/VTCFall.2018.8690852
17. M. Afshang, D. Hui, J.-F.T. Cheng, S. Grant, On phase noise compensation for OFDM operation in 5G and beyond, in *Proceedings IEEE Wireless Communications and Networking Conference (WCNC)*, pp. 2166–2171 (2022). https://doi.org/10.1109/WCNC51071.2022.9771982
18. J.-C. Sibel, Tracking the phase noise in sub-THz bands, in *Proceedings IEEE Wireless Communications and Networking Conference (WCNC)*, pp. 932–937 (2022). https://doi.org/10.1109/WCNC51071.2022.9771863
19. J.L. Hernando, A.S. Tan, A. Shojaeifard, Mitigation of Phase Noise-induced ICI at THz bands using CP-OFDM PT-RS signals, in *Proceedings IEEE Globecom Workshops (GC Wkshps)*, pp. 1766–1771 (2022). https://doi.org/10.1109/GCWkshps56602.2022.10008741
20. L.H. Nguyen, V. Braun, H. Halbauer, T. Wild, Waveform comparison under hardware limitations for 6G Sub-THz communications, in *Proceedings IEEE Annual Consumer Communications & Networking Conference (CCNC)*, pp. 1–6 (2022). https://doi.org/10.1109/CCNC49033.2022.9700588
21. Y. Li, H.-G. Ryu, L. Zhou, D. Sun, H. Liu, J. Li, Frequency offset and phase noise influence and its compensation in the DFT-spread OFDM system, in *Proceedings of International Conference on Communication, Circuits, and Systems (ICCCAS)*, pp. 52–56 (2008). https://doi.org/10.1109/ICCCAS.2008.4657726
22. V. Syrjälä, T. Levanen, M. Valkama, Methods for phase noise mitigation for DFT-S-OFDM waveforms, in *Proceedings IEEE Global Conference on Signal and Information Processing (GlobalSIP)*, pp. 660–664 (2016). https://doi.org/10.1109/GlobalSIP.2016.7905924
23. S. Bicais, J.-B. Doré, Phase noise model selection for sub-THz communications, in *Proceedings IEEE Global Communications Conference (GLOBECOM)*, pp. 1–6 (2019). https://doi.org/10.1109/GLOBECOM38437.2019.9013189
24. 3GPP: Study on new radio access technology: Radio Frequency (RF) and co-existence aspects. Technical Specification (TS) 38.803, 3rd Generation Partnership Project (3GPP) (March 2017). Release 14 version 2.0.0
25. Y. Bello, J.-B. Doré, D. Demmer, Wiener interpolation filter for phase noise estimation in sub-THz transmission, in *Proceedings IEEE 97th Vehicular Technology Conference (VTC-Spring)*, pp. 1–5 (2023). https://doi.org/10.1109/VTC2023-Spring57618.2023.10200443
26. S. Li, D. Fritsche, C. Carta, F. Ellinger, A 200-GHz sub-harmonic injection-locked oscillator with 0-dBm output power and 3.5% DC-to-RF-efficiency, in *Proceedings of IEEE Radio Frequency Integrated Circuits symposium (RFIC)*, pp. 212–215 (2018). https://doi.org/10.1109/RFIC.2018.8428978
27. M.R. Khanzadi, D. Kuylenstierna, A. Panahi, T. Eriksson, H. Zirath, Calculation of the performance of communication systems from measured oscillator phase noise. IEEE Trans. Circuits Syst. I Reg. Pap. **61**(5), 1553–1565 (2014). https://doi.org/10.1109/TCSI.2013.2285698

28. M. Sarajlic, N. Tervo, A. Pärssinen, L.H. Nguyen, H. Halbauer, K. Roth, V. Kumar, T. Svensson, A. Nimr, S. Zeitz, M. Dörpinghaus, G. Fettweis, Waveforms for sub-THz 6G: Design Guidelines. In: *Proceedings Joint European Conference on Networks and Communcation & 6G Summit (EuCNC/6G Summit)*, pp. 168–173 (2023). https://doi.org/10.1109/EuCNC/6GSummit58263.2023.10188254

29. R. Krishnan, M.R. Khanzadi, T. Eriksson, T. Svensson, Soft metrics and their performance analysis for optimal data detection in the presence of strong oscillator phase noise. IEEE Trans. Commun. **61**, 2385–2395 (2013). https://doi.org/10.1109/TCOMM.2013.042313.120670

30. S. Bicaïs, J.-B. Doré, Design of digital communications for strong phase noise channels. IEEE Open J. Veh. Technol. **1**, 227–243 (2020). https://doi.org/10.1109/OJVT.2020.2994626

31. S. Bicaïs, J.-B. Doré, J.L. Gonzalez Jimenez, On the optimum demodulation in the presence of Gaussian phase noise, in *Proceedings 25th International Conference on Telecommunication (ICT)*, pp. 269–273 (2018). https://doi.org/10.1109/ICT.2018.8464897

32. P. Desombre, H. Farès, Y. Louët, Performance comparison of digital modulations in the presence of Gaussian phase noise in the sub-THz context, in *Proceedings of International Workshop on Mobile Terahertz Systems (IWMTS)*, pp. 1–5 (2021). https://doi.org/10.1109/IWMTS51331.2021.9486786

33. S. Tarboush, H. Sarieddeen, M.-S. Alouini, T.Y. Al-Naffouri, Single-versus multicarrier terahertz-band communications: a comparative study. IEEE Open J. Commun. Soc. **3**, 1466–1486 (2022). https://doi.org/10.1109/OJCOMS.2022.3201038

34. B. Picinbono, J.-M. Kerilis, Some properties of prediction and interpolation errors. IEEE Trans. Acoust. Speech Signal Process. **36**(4), 525–531 (1988). https://doi.org/10.1109/29.1556

35. B.-J. Kwak, N.-O. Song, B. Park, D.S. Kwon, Spiral QAM: a novel modulation scheme robust in the presence of phase noise, in *Proceedings of IEEE 68th Vehicular Technology Conference (VTC-Fall)*, pp. 1–5 (2008). https://doi.org/10.1109/VETECF.2008.221

36. A.J. Viterbi, A.M. Viterbi, Nonlinear estimation of PSK-modulated carrier phase with application to burst digital transmission. IEEE Trans. Inf. Theory **29**(4), 543–551 (1983). https://doi.org/10.1109/TIT.1983.1056713

37. U. Mengali, A.N. D'Andrea, *Synchronization Techniques for Digital Receivers*, vol. 1 (Springer, Berlin, 1997). https://doi.org/10.1007/978-1-4899-1807-9

38. J. Bhatti, M. Moeneclaey, *Pilot-aided carrier synchronization using an approximate DCT-based phase noise model*, in *IEEE international symposium on signal processes and information technology (ISSPIT)*, pp. 1143–1148 (2007). https://doi.org/10.1109/ISSPIT.2007.4458068

39. A. Ugolini, A. Piemontese, T. Eriksson, Spiral constellations for phase noise channels. IEEE Trans. Commun. **67**(11), 7799–7810 (2019). https://doi.org/10.1109/TCOMM.2019.2937293

40. Y. Bello, D. Demmer, J.-B. Doré, Time domain phase noise mitigation in OFDM systems for sub-THz bands, in *Proceedings of IEEE Global Communications Conference (GLOBECOM)* (2023)

41. Y. Bello, D. Demmer, A. Hamani, A. Siligaris, C. Dehos, N. Cassiau, J.-B. Doré, J.L. González-Jiménez, Performance assessment of a 5GNR D-band CMOS transceiver with phase noise impairments, in *Proceedings of Joint European conference on networks and communications & 6G summit (EuCNC/6G Summit)*, pp. 246–251 (2023). https://doi.org/10.1109/EuCNC/6GSummit58263.2023.10188317

42. L. Pometcu, R. D'Errico, An indoor channel model for high data-rate communications in D-band. IEEE Access **8**, 9420–9433 (2020). https://doi.org/10.1109/ACCESS.2019.2960614

43. Y. Xing, T.S. Rappaport, Propagation measurements and path loss models for sub-THz in urban microcells, in *Proceedings of IEEE International Conference on Communications (ICC)*, pp. 1–6 (2021). https://doi.org/10.1109/ICC42927.2021.9500385

44. 3GPP: NR; NR and NG-RAN overall description; Stage 2. Technical Specification (TS) 38.300, 3rd Generation Partnership Project (3GPP) (September 2023). Version 17.6.0

45. F.J. Massey, The Kolmogorov–Smirnov test for goodness of fit. J. Am. Stat. Assoc. **46**(253), 68–78 (1951). https://doi.org/10.2307/2280095

46. L. Pometcu, R. D'Errico, Characterization of sub-THz and mmwave propagation channel for indoor scenarios, in *Proceedings European Conference on Antennas and Propagation (EuCAP)*, pp. 1–4 (2018). https://doi.org/10.1049/cp.2018.0991

47. L. Pometcu, R. D'Errico, Channel model characteristics in D-band for NLOS indoor scenarios, in *Proceedings of European Conference on Antennas and Propagation (EuCAP)*, pp. 1–4 (2019)

48. Y. Xing, T.S. Rappaport, Propagation measurement system and approach at 140 GHz-moving to 6G and above 100 GHz, in *Proceedings IEEE Global Communications Conference (GLOBECOM)*, pp. 1–6 (2018). https://doi.org/10.1109/GLOCOM.2018.8647921

49. J.M. Eckhardt, T. Doeker, S. Rey, T. Kürner, Measurements in a real data centre at 300 GHz and recent results, in *Proceedings of European conference on antennas and propagation (EuCAP)*, pp. 1–5 (2019)

Publisher's Note